Interlayer coupling studies of two magnetite layers across different spacers

Metselaar, J.M.

Award date:
1996

Eindhoven University of Technology
Department of Physics
Group Solid State Physics
Subgroup Cooperative Phenomena

Philips Research Laboratories
Eindhoven
Group Magnetism

Interlayer coupling studies of two magnetite layers across different spacers.

Jan Martijn Metselaar, August 1996

Report of a graduation project carried out at the group Magnetism of Philips Research Laboratories Eindhoven from July 1995 to August 1996. This project is part of a collaboration between this group and the group Cooperative Phenomena of the Eindhoven University of Technology.

Supervisors: Ir. P.A.A. van der Heijden (EUT)
Dr. P.J. van der Zaag (Philips Research)

Professor: Prof. Dr. Ir. W.J.M. de Jonge (EUT)

Abstract.

The interlayer coupling of two magnetite (Fe_3O_4) layers across different spacers has been studied. The investigated spacers were Cu, MgO, Mn_3O_4 and CoO. The samples were grown by Oxidic Molecular Beam Epitaxy. The spacer was grown in a uniform thickness and in the shape of a wedge.
The structure of the samples was characterised by X-ray diffraction. The surface structure of the Fe_3O_4 was determined by Scanning Tunnel Microscopy measurements.
The wedge shaped samples were characterised magnetically with a Magneto Optical Kerr Effect (MOKE) magnetometer, providing information on the spacer thickness dependence of the interlayer coupling. The uniform samples were investigated by means of a SQUID magnetometer, which enables temperature dependent investigation of the interlayer coupling.
A $Co_xFe_{3-x}O_4$ base layer was used to increase the coercive field of the Fe_3O_4 layer direct on top of the $Co_xFe_{3-x}O_4$. This enabled the observation of both ferro- as well as antiferromagnetic interlayer coupling.
A theoretical contemplation is given on the possible magnetic interaction mechanisms for the materials under consideration. Interactions between the magnetic ions in a material involve: RKKY, Bloembergen-Rowland, superexchange and double exchange. Interactions between two magnetic layers across a spacer involve: polarisation, tunnelling, magnetostatic coupling ('orange' peel effect), coupling across a magnetic spacer (proximity magnetism, 90° coupling) and pinholes.
Summarising the results of the studies on the coupling of two magnetite layers across a spacer, it can be concluded that:
1) Across a non-magnetic insulating MgO spacer, strong ferromagnetic coupling due to pinholes below 10 Å of MgO and weak ferromagnetic coupling above 10 Å of MgO due to 'orange peel' coupling is observed.
2) The use of a Mn_3O_4 spacer resulted in strong ferromagnetic coupling below 55 Å of Mn_3O_4, which is ascribed to proximity magnetism. Above 55 Å of Mn_3O_4 weak ferromagnetic coupling due to 'orange peel' coupling was observed. Bulk Mn_3O_4 is ferromagnetic below and paramagnetic above T_C = 42 K. Temperature dependent magnetisation measurements showed an increase in the ordering temperature of the Mn_3O_4 layer to 65 K. However, the expected spacer thickness dependence of the ordering temperature was absent.
3) Across an antiferromagnetic CoO spacer (T_N = 291 K) coupling exists below a CoO thickness of 100 Å. The nature of the coupling can not be determined by means of MOKE due to the change of preferred direction of the magnetisation of the top magnetite layer from in plane to out of plane with increasing CoO thickness for the investigated sample.
4) The use of a metallic non-magnetic Cu spacer did not show the expected polarisation effects. The measured oscillating susceptibility arises from the substrate.

Technology assessment.

The storage of information is essential to modern society. Many modern information storage media are based upon magnetism, such as, for instance, a hard disk of a computer, a video tape or the magnetic strip on a credit card. With the increasing amount of available information the need for larger and faster data storage increases. The quest for higher speed (data rate) and larger capacity leads to a reduction in the size of the structures used in the magnetic (thin film) heads and the media. Nowadays the technology is so advanced that some of the boundaries are almost set by the physical limits, notably in novel magneto-resistance sensors. It is possible to make these structures with incredible accuracy, often these structures are only a few atomic layers thick. As a result of the small dimensions, these structures exhibit interesting physical properties that are very different from bulk materials. One of the recent discoveries was the Giant Magneto Resistance effect (GMR). GMR is the large change of the resistivity of an alternating stack of thin films of certain materials depending on an applied field. This introduced new possibilities for field sensitive devices. GMR is applied in the so-called spin valve. So far the most extensively studied systems consist of metallic films. However, oxidic films are thought to be of interest in future developments. Oxidic materials in comparison to metals exhibit certain advantages such as high resistivity and good corrosion resistance. In addition, existing metallic spin valves have the disadvantage that the resistance only changes to a certain degree with an applied field, while an all oxide spin valve could in principle change from conductor to insulator with an applied field. If an all oxide spin valve were possible this would mean that the sensitivity of the thin film magnetic head would be larger. This enables the use of smaller structures in the magnetic media, which results in a higher information density.

Table of contents.

1. Introduction.

The storage of information is essential to modern society. Most modern media to store information are based on magnetism, for instance a hard disk of a computer, a video tape or a magnetic strip on a credit card. With the increasing amount of information available the need for larger and faster storage media increases. The quest for higher speed and larger capacity leads to a reduction in the size of the structures used in these media. The dimensions of these structures are limited by the technological possibilities. Nowadays the technology is so advanced that the boundaries are almost set by the physical limits. It is possible to make layered structures with an incredible accuracy, often these structures are only a few atomic layers thick. Because of the small dimensions of these structures they exhibit interesting physical properties that are very different from bulk materials. This makes it possible to create magnetic reading heads with improved properties.
This report describes the research done on thin oxidic films. So far the most extensively studied systems consist of metallic films, but oxidic films are thought to be of interest in the development of new types of magnetic heads and recording media. Some of the advantages of oxidic materials are the high resistivity and corrosion resistance.
In this chapter an introduction will be given to magnetism in general and to the use of oxidic materials in a so called 'spin valve'.

1.1 Magnetism.

Magnetism arises from the properties of the individual ions and atoms in a material. The ions and atoms can be seen as small magnetic moments or spins. The combination of these magnetic moments gives rise to the magnetic behaviour of a certain material. The ordering of the spins is determined by the interactions between the ions and atoms in a material. Several of these interaction mechanisms are described in the next chapter. In general three different magnetically ordered arrangements can be distinguished: ferromagnetic, antiferromagnetic and ferrimagnetic (Figure 1). For these arrangements the spins are ordered parallel, antiparallel and antiparallel, respectively. An antiferromagnet has no net magnetic moment because the antiparallel aligned magnetic moments cancel each other. A ferrimagnet has a net magnetic moment because of the difference in size of the magnetic moments that are antiparallel aligned.

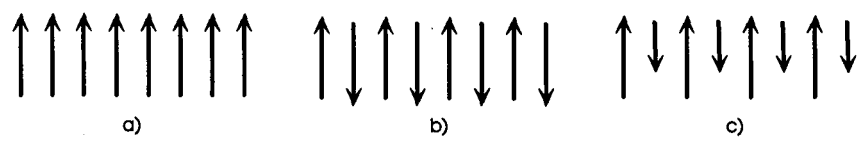

Figure 1. a) ferromagnetic ordering , b) antiferromagnetic ordering , c) ferrimagnetic ordering.

The magnetic ordering of the spins in a material occurs below a certain temperature. This temperature is different for different materials and ranges from very low, a few Kelvin, to very high, several hundreds of Kelvins.
When a ferro- or ferrimagnetic material is placed in a external magnetic field the net magnetisation will tend to align itself with the applied field. The magnetisation will only align if the applied field is sufficiently large. So when the magnetisation of a material is aligned in a certain direction, this direction can only be changed if a sufficiently large field is applied or if the ordering is destroyed because of temperature. This is used in magnetic recording media. By setting the magnetisation of small areas of a material, called domains, in a controlled manner information can be stored (for instance in a magnetic tape or disk). So by making the domains with one magnetisation direction smaller the storage capacity of a medium will increase. The information can be read from the material with a sensitive magnetic induction sensor. Increasing the capacity of a medium will require smaller and at the same time more sensitive sensors.
The studies presented here are part of the research for these induction sensors. One of these sensors is based on the so-called 'spin valve' described in the next paragraph.

1.2 The 'spin valve'.

When an electron moves through a ferromagnetic material, its mean free path depends on its spin orientation with respect to the direction of the magnetisation of the magnetic layer. A consequence of this is that an electron with its spin parallel to the magnetisation of the layer will have a different resistivity than an electron with its spin antiparallel to the magnetisation. Usually the amount of electrons with either spin direction in a material is equal. So changing the orientation of the magnetisation will have no influence on the resistivity.
The dependence of the resistivity on the magnetisation can be used in a 'spin valve' system. Consider a structure consisting of two ferromagnetic materials separated by a non-magnetic material (Figure 2).

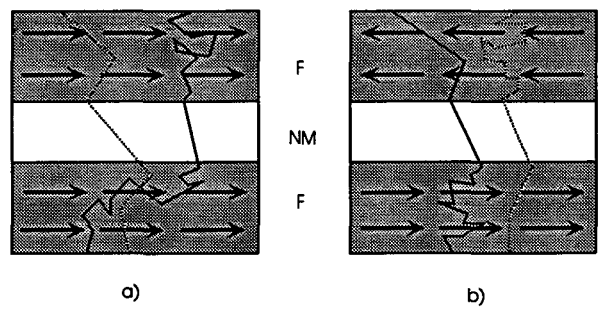

Figure 2. Representation of a spin valve. a) in the parallel state and b) in the antiparallel state. The lines represent the mean free paths of the electrons.

An electron moving through the whole structure will experience a resistivity depending on whether its spin is parallel or antiparallel to the magnetisation of the magnetic layer the electron is in. If the magnetisation of the two layers is parallel, one kind of electrons will experience a large resistivity while the other will have small resistivity. This can be

seen as two parallel channels, one with high resistivity and one with low resistivity. So according to Ohm's law the total resistivity of the structure will have a lower resistivity than the channel with the low resistivity (Figure 2a).
When the magnetisation of the magnetic layers is antiparallel both kinds of electrons will experience a high resistivity due to one ferromagnetic layer (Figure 2b). Therefore both channels have a higher resistivity than in the case of parallel magnetisation of the layers, resulting in a higher resistivity for the whole structure. This is called the 'spin valve', low resistivity: the 'open' state and high resistivity: the 'closed' state. If an external field can change the relative orientation of the magnetisation of one of the layers, the spin valve is a field sensitive device.
In *metallic* systems both spin up as well as spin down electrons contribute to the conductivity. Therefore in the antiparallel orientation of the magnetisation in a spin valve a current can still flow. Some *oxidic* materials however, conduct only electrons with one spin direction. One of these materials is magnetite or Fe_3O_4. Magnetite is a ferrimagnetic material. So two magnetite layers separated by a spacer could, in principle, be an ideal spin valve, because only if the orientation of the magnetisations is parallel the electrons are transmitted and if the orientation is antiparallel no electrons are transmitted.
A spin valve works only if the magnetisation of one of the magnetic layers can be set antiparallel to the magnetisation of the other. So the interaction (called coupling) between the magnetic layers is a point of interest. If the interaction leads to an antiparallel orientation of the magnetisation of the magnetic layers at zero field (antiferromagnetic coupling), this would mean that applying a certain field (aligning the magnetisation of the different layers in the same direction) would 'open' the spin valve and at zero field it would be 'closed'. If the layers are ferromagnetic or not coupled it will not be possible to achieve the antiferromagnetic orientation of the layers, because the layers are always parallel oriented. The antiparallel orientation can be achieved if the coercive field of the magnetic layers is different, so that the orientation of the magnetisation of one layer can be changed while the other remains fixed.
The antiparallel orientation of the magnetisation of the layers can also be achieved by fixating the magnetisation of one of the layers by coupling it directly (without a spacer) to an antiferromagnet, which is called exchange biasing.
In this report investigation of the coupling between two magnetite layers across different spacers is presented. Different interaction mechanisms will be discussed. The investigated spacer materials were Cu, MgO, Mn_3O_4 and CoO.

2. Magnetic interactions.

In this chapter an overview of several mechanisms concerning magnetic interactions will be presented. The first part is about theories which apply to coupling between two magnetic ions, while the theories in the second part specifically apply to interlayer coupling between two magnetic layers separated by a spacer.

2.1 Magnetic coupling mechanisms between two magnetic ions.

Magnetic coupling between two magnetic ions can generally be separated in direct and indirect exchange coupling. The first kind of interaction involves only two magnetic ions, while in the latter kind the interaction between the magnetic ions is mediated by one or several non-magnetic atoms or ions. Four important indirect exchange coupling mechanisms are RKKY (Ruderman-Kittel-Kasuya-Yosida), BR (Bloembergen-Rowland), Superexchange and Double Exchange interactions. The first three apply to different types of mixing of electron states of the magnetic ions mediated by non-magnetic ions. In general the RKKY theory applies to a half full electron band system (metals), while the BR and superexchange theory apply to a system with a full and an empty electron band separated by an energy gap (semiconductors, insulators). Double exchange interaction applies to materials where the interaction is mediated by electron hopping. A phenomenological description of the different coupling theories is given below. It should be noted that in the studies reported here oxidic materials are used so that the point of view here is from the oxidic side, wile most of the mechanisms described below apply to a wider range of materials.

2.1.1 Direct exchange coupling.

The direct exchange coupling between two magnetic moments s (electronspin) on neighbouring positions i,j is described by the Heisenberg Hamiltonian, H,

$$H = -2J_{ij}s_i \cdot s_j \qquad (1)$$

where J_{ij} is the exchange integral of the electronspins. The Heisenberg Hamiltonian originates from the electrostatic Coulomb forces and can effectively be described by the interaction between the electrons [1]. Consider two electronspins which can form a singlet with antiparallel spins or a triplet with parallel spins. If the two electron spin wavefunctions are orthogonal the electrons with antiparallel spin (singlet) will exhibit a symmetrical orbital wavefunction. This results in a larger probability for the electrons to be close to each other compared to the asymmetric orbital wavefunction (parallel spin, triplet). Therefore the Coulomb energy of the singlet state is larger than for the triplet state. This results in a lower energy for the parallel spin configuration or ferromagnetism. In case of non-orthogonal electronspin wavefunctions the singlet state (antiparallel spin) contributes to the binding between the ions. This contribution introduces an extra potential term in the Hamiltonian depending on the Coulomb and binding energy

resulting in ferromagnetism or antiferromagnetism. A quantum mechanical description can be found in ref. [2].

2.1.2 RKKY and Bloembergen-Rowland coupling.

The RKKY, Bloembergen-Rowland and to some extent superexchange coupling depend on the interaction between localised electrons (giving rise to the magnetic moment) of the magnetic ions and the electrons in the conductionband [2]. The localised electrons are d-electrons in the case of transition metals. The free electrons in the conductionband have a s or a p character. The interaction between these localised d-electrons and delocalised s- or p-band electrons will be called sp-d interaction. Two different sp-d interaction mechanisms can be distinguished: direct sp-d exchange and sp-d hybridisation. The difference between sp-d exchange and sp-d hybridisation is that in the first case the electrons really exchange taking each others place, wile in the latter case the electron spins interact without actually exchanging the electrons. The first mechanism originates from the coulomb potential between the d- and band electrons and can be applied to both the orthogonal as well as the non-orthogonal wavefunctions. The second mechanism originates from the overlap of the non-orthogonal wavefunctions of a d-electron and a band electron, which results in the probability of the exchange of d- and band electrons. The probability of this process will be high if the energies of the d- and band electrons are close or if the two wave functions have the same symmetry. If the energy levels lie on the same level, than the process will be resonant leading to hybridisation. Hybridisation means a mixing of the wavefunctions resulting in the broadening of the actual level.
The sp-d interactions cause coupling of the local spin of a magnetic ion to the spins of the conduction electrons. The interaction between these conduction electrons and the spin of a second magnetic ion results in an indirect interaction between the two magnetic ions. This interaction can be described with a Heisenberg Hamiltonian

$$H_{d-d} = -2\sum_{i<j} J_{ij}^{d-d} S_i \cdot S_j \qquad (2)$$

S_i, S_j are the spins of the ions at position i and j, J_{ij}^{d-d} is the effective exchange coupling constant. Depending on the sign of J_{ij}^{d-d} the coupling will be either ferromagnetic (positive) or antiferromagnetic (negative).
The sp-d interactions can be described in different ways. Here two interaction models will be discussed. The first description is based on sp-d exchange, the second description on sp-d hybridisation [3, 4]. As stated before the RKKY model applies to a situation with a metallic conductionband. A description of the RKKY model in terms of only sp-d exchange is as follows (see Figure 1): direct sp-d exchange between a local d-electron with spin s on magnetic ion i and a band electron in state $k < k_F$ with spin s' (k is the wave vector of the electron, k_F is the Fermi vector) results in an exchange of both spins (actually the electrons are exchanged). The band electron will be excited to the empty band $k'>k_F$ (II). Direct sp-d exchange of this excited electron (with spin s now) with a local d-electron with spin s' of a magnetic ion j causes another spin exchange and the band electron will return to its original state k (IV). As a result the electronspins on ion i and j are exchanged (V) and the band electron is twice scattered ($k \rightarrow k' \rightarrow k$). Similar to

direct exchange the exchange of spins corresponds with an exchange energy, only now the exchange is indirect.
A calculation of the exchange integral J for the RKKY interaction is given in ref. [2]. The interaction oscillates between ferro- and antiferromagnetic depending on the distance between the magnetic ions i and j. This is a result of the wave character of the electrons and the periodicity of the lattice, which only allows certain discrete values for the Fermi wave vector. The strength of the interaction decreases exponentially with the increasing distance between the magnetic ions.

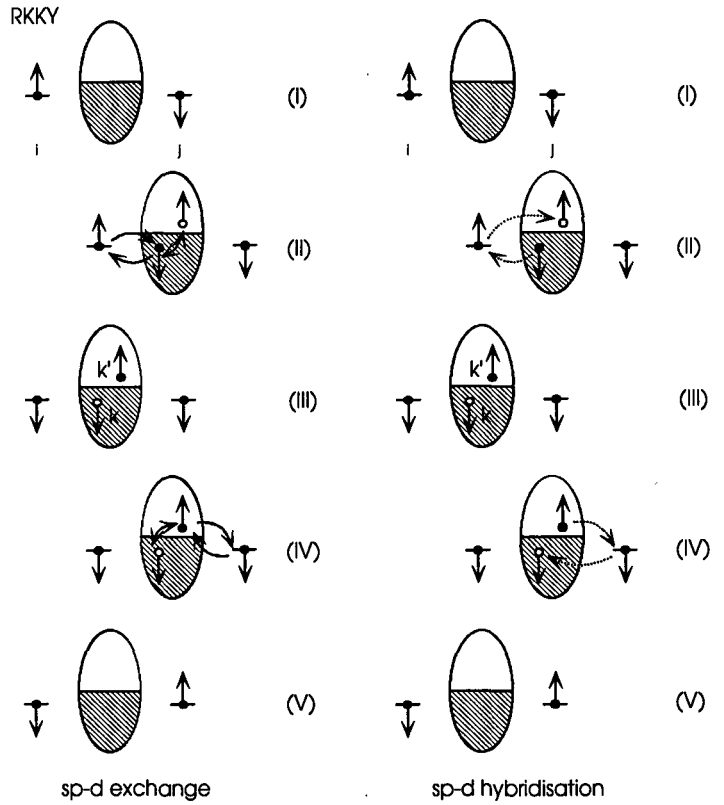

Figure 3. Schematic representation of the RKKY interactions. The arrows up and down at either side of the pictures represent the spins of the magnetic ions and the ovals the conduction band. The solid arrows represent direct sp-d exchange. The solid double sided arrows are transitions between different states and the dotted arrows are virtual transitions due to sp-d hybridisation (after [2]).

RKKY can also be described in terms of sp-d hybridisation. A schematic representation is given in Figure 3. In this case four *virtual* electron transfers take place. First a d-electron with spin s is transferred from magnetic ion i to band state $k' > k_F$ and an electron from band state $k < k_F$ with spin s' is transferred to a d-state on ion i (II). Secondly a d-electron with spin s' is transferred from magnetic ion j to band state k and the electron from band state k' with spin s is transferred to a d-state on ion j (IV). The net result is again an exchange of spin between the ions i and j (V).

The difference between sp-d hybridisation and sp-d exchange is that in the first case only the spins interact through overlap of the wave functions while in the latter case the interaction leads to the real exchange of the electrons.
The Bloembergen-Rowland model describes the interaction for semiconductors. In this case the conductionband and valenceband are separated by a small energy gap (E_g). It can be described in the same way as the RKKY interaction (Figure 4).

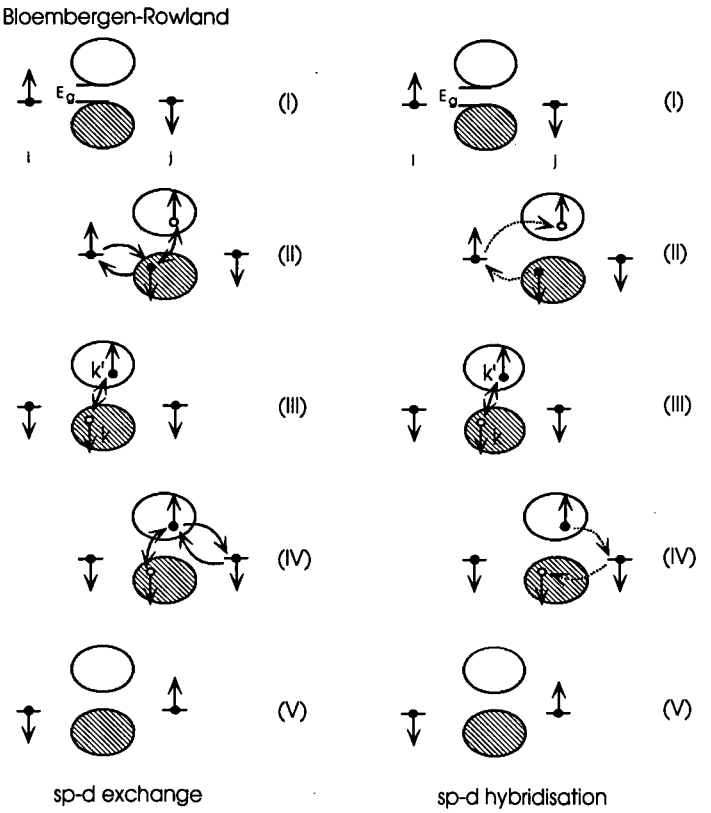

Figure 4. Schematic representation of the BR interactions. The arrows up and down at either side of the pictures represent the spins of the magnetic ions and the ovals the different electron bands. The solid arrows represent direct sp-d exchange. The solid double sided arrows are transitions between different states and the dotted arrows are virtual transitions due to sp-d hybridisation (after [2]).

Sp-d exchange between a local d-electron with spin s at position i and a valenceband electron in state *k* with spin s' results in spin exchange and excitation of the band electron to state *k'* in the conductionband (II). Direct sp-d exchange between this excited electron (with spin s) and a local d-electron with spin s' at position j results again in spin exchange and the excited electron falls back into its former state in the valenceband (IV). So as a result the local electronspins at ion i and j are exchanged (V). The difference with RKKY is that the states *k* and *k'* do not apply to the same band but to bands separated by an energy gap. For this kind of materials the Fermi level lies in the energy gap. The exchange integral J for BR interaction is similar to the one for RKKY except for the appearance of an extra exponential term [2]. This exponential term decreases the coupling strength and is proportional to the energy gap, E_g.

In the same manner as for RKKY the interactions for BR can be described in terms of sp-d hybridisation (Figure 4).

2.1.3 Superexchange coupling.

The third interaction is superexchange. This type of exchange applies to insulators, in which the energy gap is much larger than for semiconductors. Originally the model evolved from a 'three-center-four-electron' model [5]. The interaction between the magnetic ions is mediated by non-magnetic ions. The overlap of the wavefunctions of two magnetic ions and a non-magnetic anion results in the exchange of unpaired electrons on the ions with two paired electrons on the intermediate anion. The overlap is usually illustrated as in Figure 5.

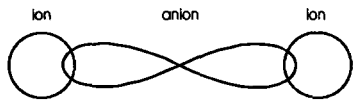

Figure 5. Illustration of the overlap of wave functions.

The RKKY and Bloembergen-Rowland theories are described in terms of a band structure. The interaction is described between the band electrons and localised electrons. In order to make the comparison with the previous theories, in the case of superexchange the intermediate ion can be associated with a sort of 'band'. One should be cautious in applying the same mechanisms to insulators because a band structure such as for metals and semiconductors can not be identified as easily. The superexchange theory can now be described in terms of sp-d exchange and sp-d hybridisation (Figure 6). Using both sp-d exchange and sp-d hybridisation the interaction is described as follows: first a virtual transition of the electron with spin s from intermediate ion A to j takes place (II). This is followed by sp-d exchange between the remaining electron with spin -s on A and the electron with spin s on i. Finally the electron with spin -s on j makes a virtual transition to A (VI). Effectively the result is that the electronspins on i and j are exchanged (VII). Superexchange can also be described using only sp-d hybridisation, here both ions i and j virtually exchange their electrons with the anion A and because this anion has two paired electrons the spins are exchanged. Note that in the case of RKKY and BR interactions the process could be described without sp-d hybridisation while in the case of superexchange sp-d hybridisation is necessary. This is a consequence of the large energy gap for superexchange in comparison to the gap for RKKY and BR. Using sp-d exchange and sp-d hybridisation, calculations for the exchange constants can be found in ref. [2]. In case of sp-d exchange in combination with sp-d hybridisation the calculations result in a ferromagnetic behaviour varying inversely with the square of the distance between the magnetic ions. When only hybridisation is involved the interaction is antiferromagnetic and varies inversely with the distance between the magnetic ions. The leading term will be antiferromagnetic because it decays slower with the distance. In both cases there is no oscillating term.

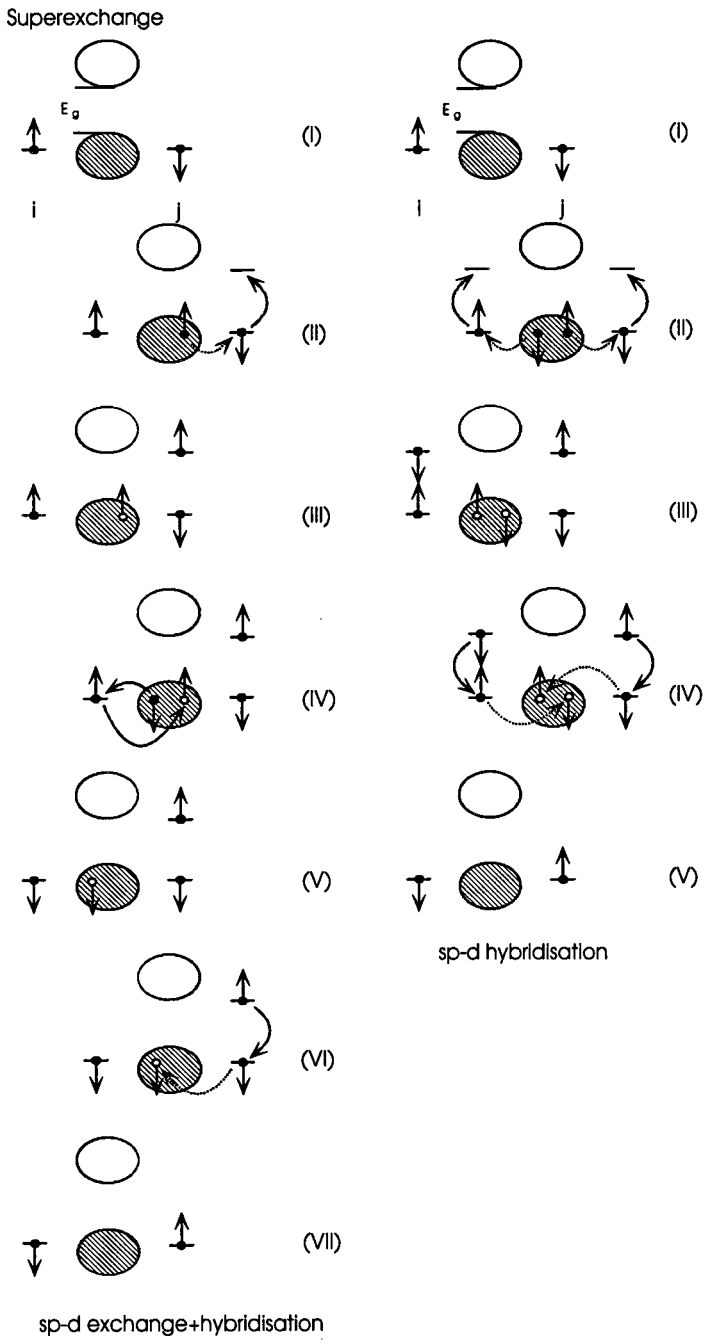

Figure 6. Schematic representation of the superexchange interactions. The arrows up and down at either side of the pictures represent the spins of the magnetic ions and the ovals represent the anion A. The solid arrows represent direct sp-d exchange. The solid double sided arrows are transitions between different states and the dotted arrows are virtual transitions due to sp-d hybridisation. (after [2]).

Different approaches to the superexchange interaction than the one above are described in ref. [6], where a review of exchange in insulators is given. Some problems concerning the calculations in the theory are summarised. Although several different ways of handling superexchange have been proposed the results all point to the same conclusions.

A solution is given in ref. [6] by separating the problem into: 1) The so called ligand field. The ligand field is the solution of the wave function of just one magnetic ion with its surroundings excluding the magnetic exchange interactions with other magnetic ions. That the exchange effects do not alter the calculated ligand field wavefunctions is significantly supported by experimental results, for instance by measurement of the hyperfine interactions of the magnetic ions with the ligand ion nuclei for dilute and concentrated versions of the same material. 2) The second part of the problem is the calculation of the magnetic interaction between the magnetic ions with the above defined ligand field wavefunctions. The magnetic interactions (exchange interactions) are involved as small perturbations on the Hamiltonian of the ligand field wavefunctions. This separation of the problem makes the calculation simpler. The actual calculation and discussion of the ligand field approach is beyond the scope of this report.
In ref. [7] a more recent explanation for superexchange interactions is shown. Here the cation-anion-cation three-center model is described taking into account all the possible exchange mechanisms between the cations across the anions. This leads to one theory bringing all different explanations of superexchange together. The various contributions to superexchange due to different interaction mechanisms are discussed and estimates of the exchange constants are given. The theory is applicable to insulating and semiconducting transition metal and rare-earth compounds. From this theory follows that the exchange takes place predominantly on the anion for transition metal compounds, while for rare-earth compounds the exchange takes place almost predominantly on the cations.

2.1.4 Double exchange coupling.

The mechanism for double exchange coupling is based on the presence of electrons able to hop from one magnetic ion to another magnetic ion. The hopping electrons, carriers of spin, have an effect on the magnetic interactions between the magnetic ions resulting in ferromagnetic coupling. This was first explained in ref. [8]. Consider a system for which the intra-atomic exchange is strong so that the spin of each carrier is parallel to the local ionic spin and the carriers do not change their spin when hopping. Thus an electron can only hop from ion to ion if its spin is parallel to the spin of the ions. When hopping is possible the groundstate energy is lowered because the electrons can participate in the binding. This results in a lower energy for ferromagnetic spin configurations. From the above it is clear that the angle between the adjacent spins of the ions must play an important role in the process of double exchange.
A calculation of the spin configuration using a simplified physical model is given in ref. [9] and will be summarised here. The exchange energy and the angle between the spins are calculated.

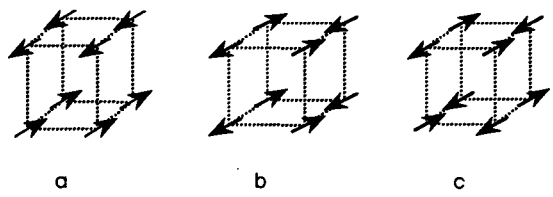

Figure 7. Different antiferromagnetic configurations on a simple cubic lattice. a) 'layer', b) 'chain' and c) 'alternating' antiferromagnet.

Consider a material with a small amount of hopping electrons,x, at low temperatures. Assume an antiferromagnet of the 'layer' type (Figure 7a). Each electron spin of length S is coupled ferromagnetically to z' neighbouring spins within the layer and antiferromagnetically to z spins in the adjacent layers. The exchange integrals between these spins are called J' (>0) and J (<0) respectively. The exchange energy between the ionic spins is

$$E_{ex} = -Nz'\,J'\,S^2 + Nz|J|S^2\left(2\cos^2(\theta_0/2)-1\right) \qquad (3)$$

where N is the number of ions per unit volume and θ_0 the angle between the magnetisations of the successive layers. In principle the carriers are able to hop to all neighbouring ions, both in the layers as well as in the adjacent layers. The probability is given by the transfer integrals b' and b respectively. If $b << |J|S$ the energy of a carrier is given by

$$E_m = -z'\,b' - zb\cos(\theta_0/2) \qquad (4)$$

The total number of carriers per unit volume is given by Nx (x<<1) so that the total contribution to the double exchange by these carrier electrons is

$$E_d = NxE_m \qquad (5)$$

The total magnetic energy $E=E_{ex}+E_d$ can be minimised with respect to θ_0 resulting in an angle, θ_0, between the magnetisation of the adjacent layers given by

$$\cos(\theta_0/2) = bx/4|J|S^2 = \xi \qquad (6)$$

with a minimal energy of

$$E = E_{ex} + E_d = N\left(-z'\,J'\,S^2 - xz'\,b' - z|J|S^2 - (z/8)b^2x^2/|J|S^2\right) \qquad (7)$$

The result is that because of the double exchange mechanism the spins of adjacent layers are not antiparallel (θ_0=180°). For $\xi \leq 1$ a canted spin configuration will be formed. If $\xi >$ 1 (θ_0=0°) the spin configuration is ferromagnetic. An angle, θ_0, could result in a random orientation of the sublattice spins. Due to anisotropy forces a two-sublattice arrangement will in general be favoured which results in a non-zero magnetisation. The above calculations apply to a 'layer' type of antiferromagnet (Figure 7a). Hopping is also allowed in the 'chain' or 'alternating' type of antiferromagnet (Figure 7b,c). A similar calculation as the one above can be made for these kind of spin arrangements which also results in a

canted spin structure. The main difference is that now more than two sublattices may have to be considered.
One of the assumptions made in the above given model was the low temperature limit. At non-zero temperatures the spins start to fluctuate with increasing temperature, which results in different decreasing rates for E_{ex} and E_d. Since E_{ex} is proportional to $\cos^2(\theta_0/2)$ and E_d to $\cos(\theta_0/2)$ the calculated spin structure will change and the angle of canting will decrease leading to either a ferromagnetic or an antiferromagnetic ordering [6]. Figure 8 shows a phase diagram indicating the stable regions for the different spin configurations as a function of temperature and carrier concentration. The transition points T_1, T_N, T_C are complicated functions of the various parameters.

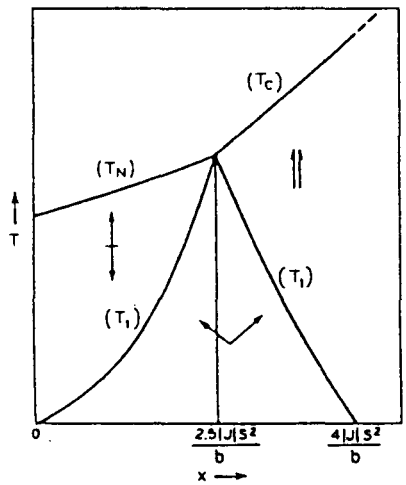

Figure 8. Phase diagram for a double exchange material, showing the stable regions of canted, ferromagnetic and antiferromagnetic spin configurations, after [9].

An other assumption made in the derivation above is that the carriers are free to hop through the lattice. In the case of localised carriers, where the carriers are not free and only interact with their close surroundings, it can be shown that local canting will appear. The (long range) superexchange interactions present through the lattice tend to couple the local distortions together and the resulting arrangement is the same as if the carriers were free.
Double exchange is a process occurring in materials such as oxides, for example Fe_3O_4, in which the electron transport is hopping type. In these materials the magnetic interaction mechanism is often superexchange, so if double exchange is possible it will have to compete with superexchange. This is something which has to be noted, not just one coupling mechanism has to apply to a system. To describe the whole picture it might be necessary to take different mechanisms into account and it depends on the materials characteristics which mechanism is dominant.

2.2 Interlayer exchange coupling mechanisms.

This part of the theory concerns the coupling of two magnetic layers across a spacer. Several interactions of different origins will be discussed. The first two, tunnelling and polarisation apply to systems composed of metals and insulators (hybridic systems). The other three: magnetostatic coupling, coupling across a magnetic spacer and pinholes can be applied more general.

2.2.1 Tunnelling.

Two ferromagnetic conductors can be coupled magnetically by the transmission of electrons from one conductor to the other through an insulating spacer [10]. A mathematical description in one dimension of this coupling is given here. The one-electron Hamiltonian, H_ξ, in one dimension is given by

$$H_\xi = \frac{-\hbar^2}{2m}\left(\frac{d}{d\xi}\right)^2 + U(\xi) - h(\xi)\cdot\sigma \qquad (8)$$

The three terms on the left in equation (8) represent the kinetic energy, the potential and the internal exchange energy respectively. The internal molecular field, $\vec{h}(\xi)$, causes the exchange splitting between the spin up and spin down electrons. $\vec{\sigma}$(=2s) is the conventional Pauli spin operator. The effective electron (or hole) mass is given by m. ξ represents the position along the axis (Figure 9).

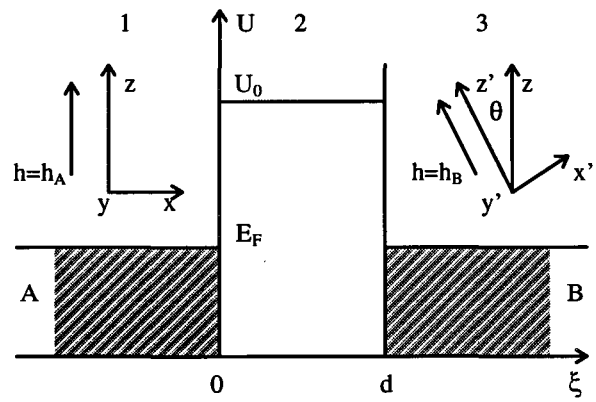

Figure 9. Schematic potential for two ferromagnets separated by an insulating barrier.

In this tunnelling model a rectangular potential barrier is assumed with $U=U_0$ for $0<\xi<d$ and $U=0$ elsewhere (Figure 9). The barrier is assumed to be non-magnetic thus $\vec{h}=0$. The ferromagnets A and B have identical material properties and therefore $\vec{h} = \vec{h}_A$ or $\vec{h}_B$ is constant with $|\vec{h}_A| = |\vec{h}_B| = h_0$. However the directions of $\vec{h}_A$ or $\vec{h}_B$, as well as the corresponding spin quantisation axis z and z' differ by an angle θ (Figure 9). Inside the ferromagnets the one-electron energy, E_ξ, is

$$E_\xi = \frac{\hbar^2}{2m} k_\sigma^2 - \sigma h_0, \qquad \sigma = \pm 1 \tag{9}$$

where k_σ is the electron wave vector $k_\sigma = \sqrt{\frac{2m}{\hbar^2}\left(E_\xi + \sigma h_0\right)}$ (The notations $\sigma = \pm 1$ and $\sigma = \uparrow, \downarrow$ will be used interchangeably henceforth).

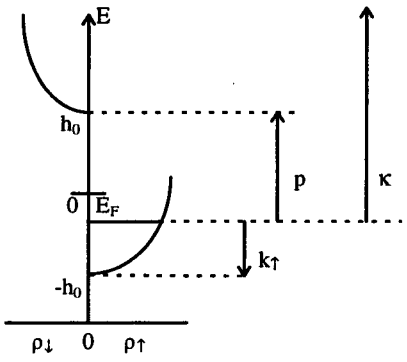

Figure 10. Density of spin up ($\rho\uparrow$) and spin down ($\rho\downarrow$) electrons.

The density of states $\rho\uparrow\downarrow$ has the schematic form shown in Figure 10. Inside the barrier the energy is

$$E_\xi = -\frac{\hbar^2}{2m} \kappa_\sigma^2 + U_0, \qquad \sigma = \pm 1 \tag{10}$$

where $i\kappa_\sigma = \sqrt{\frac{2m}{\hbar^2}\left(E_\xi - U_0\right)}$ is the imaginary electron wave vector.

The mathematical solution of the problem stated above has been performed in ref. [10]. The electron wave transmittivity across the barrier potential is calculated. It appears that the transmittivity depends on the relative orientation of the magnetisation of the ferromagnetic layers. This spin dependent tunnelling probability of the electrons results in an effective Heisenberg coupling energy given by

$$W = -J\cos\theta \tag{11}$$

where the coupling constant J can be written as

$$J = J_0 \frac{e^{-2\kappa d}}{d^2} \tag{12}$$

and J_0 is given by

$$J_0 = (U_0 - E)\frac{\kappa^2 k_\uparrow (k_\uparrow^2 - \kappa p)}{\pi^2 (\kappa^2 + k_\uparrow^2)^2 (\kappa + p)} \tag{13}$$

where κ, $k_{\uparrow,\downarrow}$ are the wave vectors determined by equation (9,10) and $p = -ik$ (Figure 10). In Figure 11 the reduced Heisenberg exchange coupling, $\frac{J_0 8\pi^2}{U_0 - E_F}\left(\frac{\kappa^2}{k_\uparrow^2}\right)$, is plotted versus the reduced barrier height ($\kappa^2/k^2{\uparrow}$).

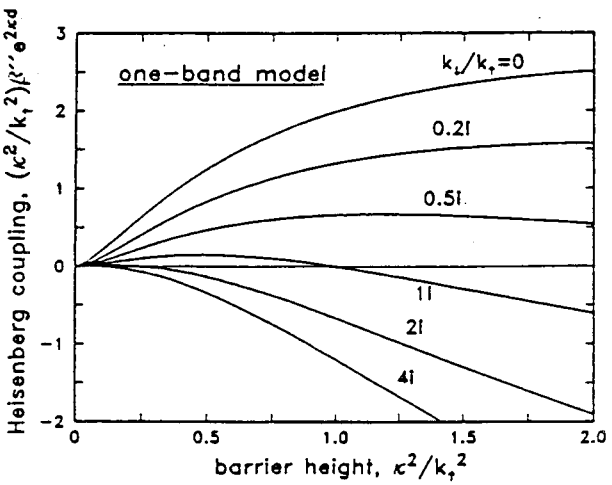

Figure 11. Reduced Heisenberg exchange coupling plotted versus the reduced barrier height $\kappa^2/k^2{\uparrow}$.

Equation (13) shows that the sign of the coupling (ferro- or antiferromagnetic), determined by the wave vectors (or energies) of the electrons ($k{\uparrow}^2$-κp), depends on the barrier height and the Fermi level in the magnetic layers. Notice that the coupling does not have an oscillatory character.

2.2.2 Polarisation.

Now consider the opposite system as the one for tunnelling: two insulators separated by a conductor. This paragraph is not directly related to the other paragraphs describing magnetic interactions because polarisation does not lead to magnetic coupling, but this type of interaction has also been investigated.
Figure 12 shows a schematic representation of two insulators separated by a conductor in one dimension. This system can be considered as a quantum well. The free electrons in the conductor are confined to the quantum well. The energy of the electrons, E_n, is quantified to discrete energy levels given by

$$E_n = \frac{\hbar^2}{2m}\left(\frac{n\pi}{L}\right)^2 \qquad (14)$$

where n is the number of the energy level, L the with of the quantum well.

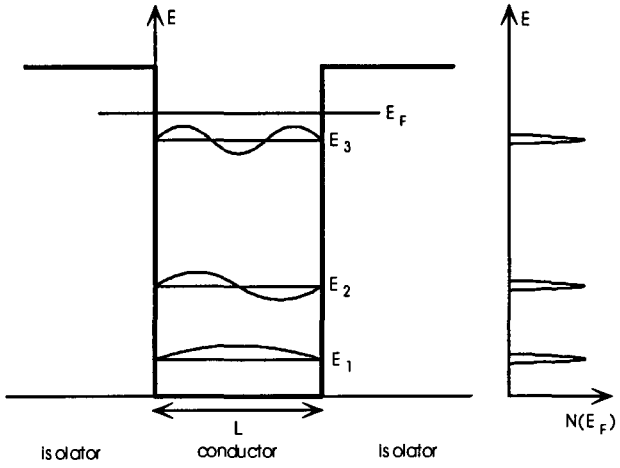

Figure 12. Schematic representation of a quantum well: two insulators separated by a conductor. On the right the density of states as a function of energy is depicted.

The number of levels below the Fermi level in the well depends on the width of the well. Each energy level corresponds to a peak in the density of states, N(E), in the well. Increasing L will also increase the number of peaks of the density of states inside the well (Figure 12). To fit an extra level in the quantum well it has to be broadened by an amount, Λ, which can be equated from

$$\frac{\hbar^2}{2m}\left(\frac{n\pi}{L}\right)^2 = \frac{\hbar^2}{2m}\left(\frac{(n+1)\pi}{L+\Lambda}\right)^2 \qquad (15)$$

With $n\pi/2 = k_F$ (the fermi wave vector), for large L (and n) Λ is given by

$$\Lambda = \frac{\pi}{k_F} \qquad (16)$$

When a field is applied to a paramagnetic conductor the spin up and spin down electron energy levels will split up due to the Zeeman effect (Figure 13).

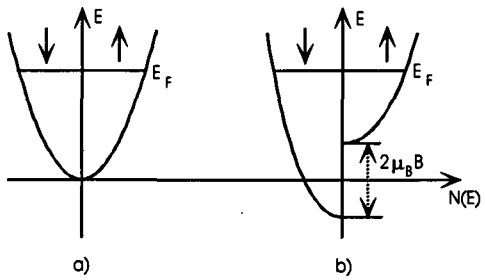

Figure 13. Zeeman splitting of the energy levels of the spin up and down electrons. a) no applied field, no splitting. b) Zeeman splitting due to an applied field.

The magnetisation, M, of a paramagnetic material is given by

$$M = \mu_B^2 N(E_F) B \qquad (17)$$

where B is the applied field. The quantity $\mu_B{}^2N(E_F)$ is called the paramagnetic Pauli susceptibility, χ^{Pauli}. The magnetisation is proportional to the density of states at the Fermi level, $N(E_F)$. For a quantum well the density of states at the Fermi level of the paramagnetic spacer depends on width of the well (equal to the spacer thicknesses) and therefore the magnetisation of the spacer will also depend on its thickness. The density of states at the Fermi level peaks at discrete values of the spacer thickness, so that the magnetisation will have an oscillatory character with the spacer thickness, the magnetisation is zero unless $E_F = \frac{\hbar^2}{2m}\left(\frac{n\pi}{L}\right)^2$.

For a system with two ferrimagnets as insulators the hysteresis loop is composed of the magnetic contribution of the ferrimagnetic layers and the paramagnetic spacer. In the case of zero saturation field of the ferrimagnets the hysteresis loop measured by MOKE rotation, θ_K, (which is proportional to the magnetisation) is given by

$$\theta_K(B) = C\left(M_s + \chi^{Pauli} B\right), \quad B > 0 \qquad (18)$$

where CM_s is the saturation Kerr rotation (arising from the ferrimagnets) and $C\chi^{Pauli}B$ the rotation due to the polarisation. The oscillations can be observed in a change of the slope of the hysteresis loops measured with MOKE. Figure 14 shows an example of the loops measured for such quantum well systems [11].

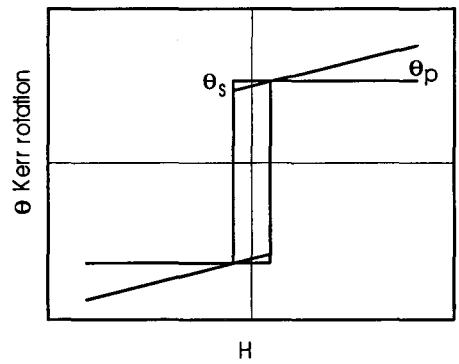

Figure 14. Example of two hysteresis loops one without and one with polarisation: θ_s is the contribution of the ferrimagnets and θ_p the contribution due to polarisation (after [11]).

2.2.3 Magnetostatic coupling.

In ref. [12,13] the magnetostatic coupling arising from correlated interface roughness is described and is called the 'orange peel' effect. Consider two ferromagnetic layers separated by a non-magnetic spacer. If, as in an orange peel, the interfaces have small irregularities each hump or depression constitutes to a small magnetic dipole. These dipoles on each side of the spacer interact with each other depending on the correlation of the irregularities. In the case of positively correlated interface roughness (Figure 15) each

dipole is interacting with its counterpart on the other side of the spacer tending to align parallel giving rise to ferromagnetic coupling. The parallel alignment is most favourable because the flux lines are continuous as is shown by the dotted line in Figure 15.

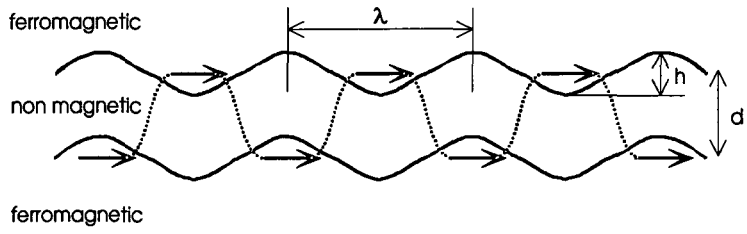

Figure 15. An example of positively correlated interface roughness of two ferromagnetic layers separated by a non-magnetic layer.

In ref. [12,13] calculations of the magnetic coupling energy are performed. The interface roughness is modelled by a sinusoidal shape represented by

$$z = h\sin\left(\frac{2\pi x}{\lambda}\right)\sin\left(\frac{2\pi y}{\lambda}\right) \qquad (19)$$

where z is the direction perpendicular to the plane of the interface and x,y the orthogonal directions in the interface plane. λ is the period and h the amplitude of the roughness (Figure 15). In this case the coupling constant J for two identical magnetic layers is

$$J = -\frac{\pi^2 h^2}{\sqrt{2}\lambda}\mu_0 M^2 e^{-\frac{2\pi\sqrt{2}d}{\lambda}} \qquad (20)$$

where d is the average distance between the two magnetic layers and M is the magnetisation of the layers.
If the interfaces are not correlated ideally the coupling strength will be smaller. Magnetostatic coupling can also lead to a non zero angle between the magnetisations of the magnetic layers. In ref. [14] a system of one perfectly flat interface and a stepped surface is considered. The magnetic dipole field created by the steps is calculated. Minimisation of the magnetic energy of the system leads to a 90° angle between the magnetisations of the two magnetic layers. The coupling strength depends on the height and the width of the steps. For an interface with a non-perfect correlated step array the results are similar.

2.2.4 Coupling across a magnetic spacer.

Consider a system build up by several magnetic materials, thus using a magnetic spacer in stead of a non-magnetic spacer. The materials can exhibit the same or different types of magnetic ordering (ferromagnetism, ferrimagnetism or antiferromagnetism). The magnetic interaction at the interface between the different materials will determine the magnetic behaviour of the total system. First consider two ferrimagnets, with different magnetic properties, on top of each other. If the structural lattice and magnetic ordering of

the materials is the same the spins at the interface will be coupled and the magnetic structure is continued across the interface resulting in ferromagnetic coupling between the layers. The magnetic behaviour of the total system depends on the individual magnetic properties of both layers. In case of similar magnetic properties and / or thin layers, the system will behave as one magnetic entity. The magnetic properties of the entity are the weighed average of the magnetic properties of the separate materials. This can be used to manipulate the magnetic properties of a layer. An example of the behaviour for a system composed of thick ferrimagnetic layers with a large difference between the magnetic properties is given in ref. [15].
The interface between the two materials does not have to be perfectly flat to exhibit the behaviour described above. In Figure 16 a schematic representation is given of two ferrimagnets on top of each other. It shows that roughness does not have to lead to a large reduction of the magnetic coupling at the interface. As long as the magnetic structure is continuous across the interface magnetic coupling will exist.

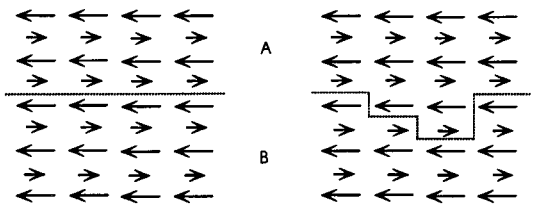

Figure 16. Two ferrimagnets A,B on top of each other. Left with perfect interface, right with interface roughness.

Now consider a stack of three magnetic layers: two ferrimagnets separated by a magnetic spacer. The first type of spacer is an antiferromagnet. At the interface of a ferri- and an antiferromagnet the spins of the antiferromagnet will only couple to the spins of one of the sublattices of the ferrimagnet. Coupling over a perfectly flat antiferromagnet will cause the magnetisation of the top and bottom layer to be alternating parallel to antiparallel with the addition of each monolayer of the spacer (Figure 17).

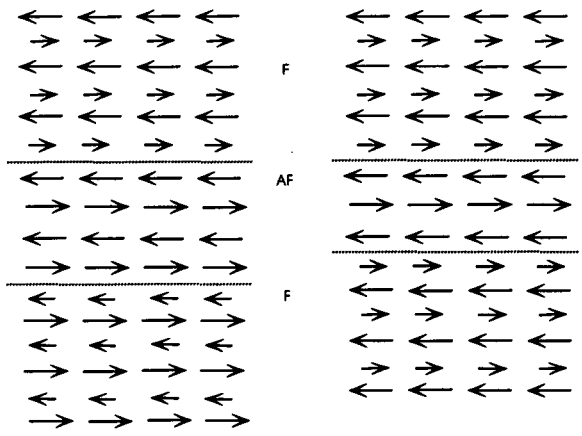

Figure 17. Schematic representation of two ferrimagnets separated by an antiferromagnet, left antiparallel situation, right parallel situation.

Some degree of interface roughness will still lead to coupling although not alternating ferro- / antiferromagnetic. The coupling energy can be written as

$$W = C_+(\theta)^2 + C_-(\theta - \pi)^2 \qquad (21)$$

where the coupling coefficients C_+, C_-, which can only be positive, represent the mean contribution of the parts of the spacer favouring the parallel or antiparallel orientation respectively and θ is the angle between the magnetisations of the two magnetic layers. If neither one of these constants vanishes, the orientation of the magnetisation of the ferromagnetic layers will not be linear (that is $\theta = 0^\circ$ or 180°). Minimising (22) results in a value for θ of

$$\theta = \frac{C_-\pi}{C_- + C_+} \qquad (22)$$

So if C_- equals C_+ the favourable configuration of the magnetisation will be orthogonal [16]. This type of coupling is called 90° coupling.

The second case of a magnetic interlayer is a paramagnet separating the two magnetic layers. In a paramagnet the ions are not non-magnetic, but their interaction is to small to result in a magnetic ordering. At the interface between the ferrimagnetic material and the paramagnetic material the paramagnetic electron spins will experience a magnetic interaction with the electron spins of the ferrimagnet. The spin structure at the interface of the paramagnet is stabilised by the presence of the ferrimagnet. The first ordered layer of the paramagnet can induce a next ordered layer and so on. This phenomenon is called proximity magnetism and leads to coupling between the ferrimagnets [16]. Factors influencing proximity magnetism could be strain in or non-stochiometry of the paramagnet, which changes the spin structure.

2.2.5 Pinholes.

Pinholes are bridges between the magnetic layers across the spacer material. These bridges occur when the growth of the stack is not perfect. Growth of a *thin* spacer on top of a magnetic layer will not completely cover the surface of the magnetic layer because of interface roughness. The second magnetic layer, grown on top of the spacer will than be in direct magnetic contact with the first magnetic layer (Figure 18). The direct contact of the magnetic layers caused by pinholes results in ferromagnetic coupling.

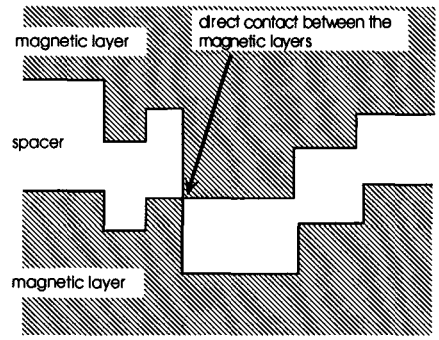

Figure 18. Pinhole by touching magnetic layers due to interface roughness.

2.3 Summary.

In conclusion to this chapter it should be stressed that the general mechanisms described here can occur simultaneously in one system. The total magnetic interaction is the addition of all magnetic coupling effects present in a certain system.

Table 1 gives a survey of the discussed coupling mechanisms.

Table 1. Survey of the coupling mechanisms.

Type of coupling	Character	Application
coupling between magnetic ions:		
Direct Exchange	ferromagnetic	metals
RKKY	oscillating ferro- or antiferromagnetic	metals
BR	oscillating ferro- or antiferromagnetic	semiconductors
Superexchange	antiferromagnetic	insulators
Double Exchange	ferromagnetic	hopping type conductors

Type of coupling	**Character**	**Application**
interlayer exchange coupling:		
Tunnelling	ferro- or antiferromagnetic	hybridic systems
Polarisation	no coupling	hybridic systems
Magnetostatic coupling	ferromagnetic or 90° coupling	general
Coupling across a magnetic spacer	ferro- ,antiferromagnetic or 90° coupling	general
Pinholes	ferromagnetic	general

3. Structure and magnetic properties of several oxides.

In this chapter the structure and magnetic properties of Fe_3O_4 (magnetite), Mn_3O_4, MgO and CoO are discussed. The first paragraph describes the rocksalt and spinel structure. In the next two paragraphs the properties of Fe_3O_4 and Mn_3O_4 are discussed. The last paragraph treats the mono-oxides MgO and CoO.

3.1 The spinel and rocksalt structure.

In nature a wide variety of crystal structures is found. One of the simplest forms is the rocksalt structure (Figure 19). The rocksalt structure consists of two f.c.c. sublattices which are shifted half a lattice parameter with respect to each other. NaCl (rocksalt) crystallises in this structure.

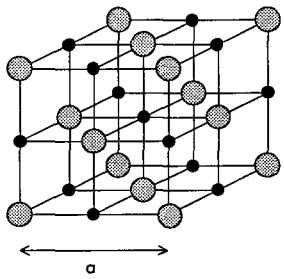

Figure 19. The rocksalt structure consists of two f.c.c. sublattices (grey spheres and black spheres) which are shifted half a lattice parameter, a, with respect to each other.

A more complicated crystal structure is the spinel structure (Figure 20). $MgAl_2O_4$ is the prototype of the material which crystallises in the spinel-type structure. A spinel unit cell consists of eight octants with one f.c.c. oxygen configuration, so one unit cell contains 32 oxygen atoms. The other ions are positioned at two different sites, the tetrahedral or A sites surrounded by 4 oxygen ions and the octahedral or B sites surrounded by 6 oxygen ions.

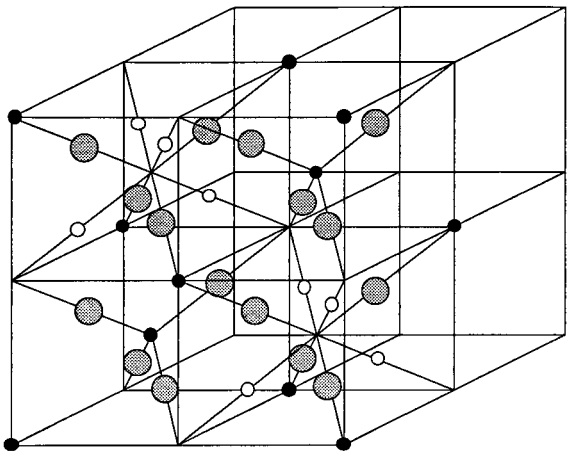

Figure 20. The unit cell of a spinel structure. One unit cell consist of eight octants. The large grey spheres represent the oxygen atoms, the small black spheres represent the tetrahedral or A sites and the white spheres represent the octahedral or B sites.

3.2 Properties of Fe_3O_4.

The structure of magnetite is the inverse spinel structure. The magnetite unit cell contains 8 divalent and 16 trivalent iron ions (cations). In the inverse spinel structure the divalent ions (8 Fe^{2+}) occupy 8 of the 16 available octahedral sites, in contrast to the normal spinel structure in which the divalent metal ions occupy the 8 available tetrahedral sites. The trivalent ions (16 Fe^{3+}) are distributed over the remaining sites. The chemical formula for this distribution is $Fe^{3+}[Fe^{2+}Fe^{3+}]O_4$, with between the brackets the ions at the B sites. The cation distribution in a certain spinel is determined by factors such as the ion size, Coulomb energy of the charged ions, crystal field etc. [17]. The f.c.c. oxygen sublattice has a lattice parameter of 4.2 Å. The total lattice parameter of one Fe_3O_4 unit cell is 8.40 Å.

The magnetic ordering in Fe_3O_4 is ferrimagnetic and the magnetic moment can be calculated from the spin arrangement of the iron ions. The Fe^{3+} ions have 5 electrons in their 3d shell. According to Hund's rule the electrons prefer a parallel alignment of their spins, resulting in a total spin of 5/2. The Fe^{2+} ions have 6 electrons in their 3d shell. Only 5 electrons are allowed to be in a state with the same spin direction, according to Pauli's exclusion principle. The remaining electron will have its spin antiparallel with respect to the other electrons resulting in a total spin of 2.

Superexchange is the dominant magnetic interaction mechanism. If the oxygen ion is exactly in between the iron ions, the overlap of the wavefunctions between the oxygen and iron ions will be largest, because the oxygen 2p orbital is stretched out in two opposite directions. If the oxygen ion is not exactly in the middle the interaction will be smaller and, in principle, zero if the angle between the iron-oxygen-iron ions is 90°. In magnetite the bond angle of A-O-B is about 125°, for A-O-A it is 80° and for B-O-B it is 90° so that the A-O-B interaction is the dominant interaction. Superexchange interaction is antiferromagnetic thus leads to antiparallel alignment of the spins on the A and B sites.

The spins on the A (or B) sites are parallel aligned. Since there are as many Fe^{3+} on A sites as on B sites their moments will cancel, the net magnetisation arises only from the Fe^{2+} ions. The Curie temperature is 585 K, above which Fe_3O_4 becomes a paramagnet. Electron hopping of an electron from a Fe^{2+} to a Fe^{3+} at the B sites gives rise a half metallic conduction character and to a double exchange contribution, resulting in an extra contribution to the parallel alignment of the spins at the B sites. A detailed description of the properties of Fe_3O_4 is given in ref. [17].

3.3 Properties of Mn_3O_4.

The structure of Mn_3O_4 is of the hausmanite type. Hausmanite is a tetragonally distorted spinel structure. This means the spinel unit cell is stretched along the z direction (Figure 21). For the hausmanite structure $a = b \neq c$, in contrast to the spinel structure, where $a = b = c$. At room temperature the lattice parameter of the unit cell, A, is 5.7621 Å ($a = A\sqrt{2} =$ 8.1488 Å) and $c = 9.4699$ Å.

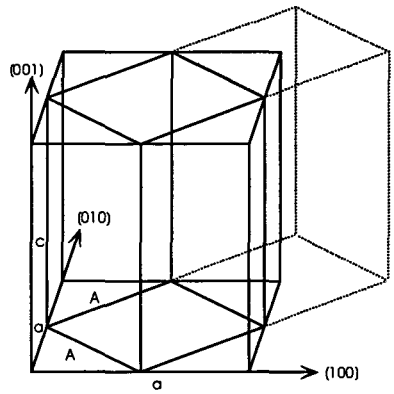

Figure 21. The hausmanite structure with $a = b \neq c$. Notice the orientation of the unit cell. The magnetic unit cell is twice the chemical unit cell, doubled along the [110] direction (after [18]).

The ionic distribution is described by the chemical formula $Mn^{2+}[(Mn^{3+})_2]O_4$ so that the 8 Mn^{2+} ions occupy the tetrahedral sites and the 16 Mn^{3+} ions occupy the octahedral sites in one unit cell. The Mn^{3+} have 4 electrons in their 3d shells with their spins parallel aligned, resulting in a total spin of 2. The Mn^{2+} ions have 5 electrons in their 3d shells which are also parallel aligned resulting in a total spin of 5/2. The iron ions are separated by oxygen ions so that the superexchange interaction is the dominant magnetic mechanism. This causes an antiparallel alignment of the net magnetisation of the A and B sites. However, the tetragonal distortion of the spinel lattice reduces the overlap of the wavefunctions in the A-O-B configuration. Furthermore, in contrast to Fe_3O_4, electron hopping and therefore a double exchange interaction between the B sites is absent. This results in a competition between the antiferromagnetic A-O-B and B-O-B interaction giving rise to a canted spin structure at the B sites. The schematic representation of the structure is given in Figure 22. This diagram was constructed from neutron diffraction experiments [19]. The magnetic unit cell in the ordered phase is orthorhombic and

contains two chemical unit cells. The spin structure still results in a net magnetisation, thus Mn_3O_4 is a ferrimagnet. The Curie temperature for Mn_3O_4 is 41.9 K [20], above which Mn_3O_4 becomes a paramagnet.

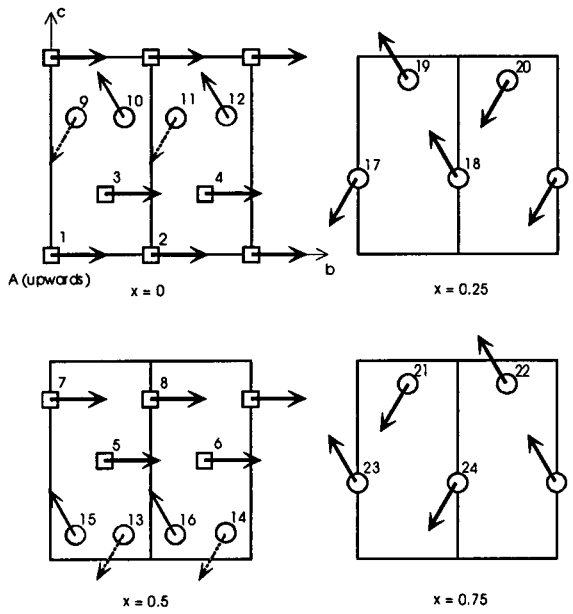

Figure 22. The magnetic structure for Mn_3O_4 at 4.7 K. The squares represent tetrahedral sites, the circles octahedral ones. The thick solid horizontal arrows represent moments in plane. The thin solid arrows represent moments directed upwards and the dotted arrows moments directed downwards. x is the position along side A (after [19]).

3.4 Properties of MgO and CoO.

MgO and CoO all have a rocksalt structure. These materials have got a chemical unit cell with lattice parameters: 4.20 Å and 4.26 Å for MgO and CoO respectively, which is twice as small as the unit cell for magnetite. The oxygen forms a f.c.c. lattice with about the same lattice constant as the f.c.c. oxygen lattice of the spinel structure. All three of these materials are insulators. MgO is a non-magnetic material. CoO is an antiferromagnet with a Néel temperatures of 291 K. The antiferromagnetic character arises from the superexchange interaction of the spins of the metal ions with their six surrounding metal ion neighbours mediated by the oxygen ions. Due to the rocksalt structure the magnetic moments of the individual ions cancel each other completely in the ordered phase, so that CoO is an antiferromagnet. In Figure 23 an impression is given of the magnetic structure of CoO. The magnetic unit cell for CoO is twice as large as the chemical unit cell. CoO also changes from the rocksalt structure, below T_N it is tetragonally contracted ($a = b \neq c$) along the [100] axis with $c/a = 0.998$ [21].

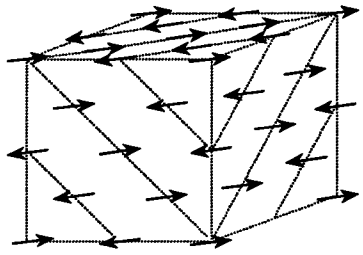

Figure 23. Magnetic structure of CoO, for clarity the oxygen atoms have been omitted.

3.5 Summary.

The structure and properties of the different materials are summarised in Table 2.

Material	a [Å]	d [g/cm^3]	T_C / T_N [K]	Spin order	ρ [Ω cm] at 300 K	M_s [kA/m]
Fe_3O_4	8.398	5.2003	860	F	$5 \cdot 10^5$	496 (T=293 K)
Mn_3O_4	a= 8.149 c=9.470	4.873	41.9	F	10^{15}	215 (T=4.7 K)
MgO	4.212	3.5837	-	-	-	-
CoO	4.260	6.45	291	AF	10^{10}	0
$MgAl_2O_4$	8.080	3.583	-	-	-	-

Table 2. Properties of different oxides. The value for M_s of Fe_3O_4 is found in ref. [17], of Mn_3O_4 in ref. [20]. The values for the resistivity can be found in ref. [22].

4. Experimental procedures.

In this chapter the experimental techniques used to characterise the structural and magnetic properties are presented. In the first part of this chapter the growth and structural characterisation of the samples is discussed. The second part describes the magnetic characterisation. The majority of the magnetic studies were done using the Magneto Optical Kerr Effect (MOKE). The third part of the chapter deals with the interpretation of the measurements.

4.1 Growth and structural characterisation.

4.1.1 Oxidic Molecular Beam Epitaxy.

The samples used were grown using an Oxidic Molecular Beam Epitaxy system (Oxi-MBE). The apparatus used is a differentially pumped UHV Balzers UMS 630 multichamber MBE system (Figure 24).

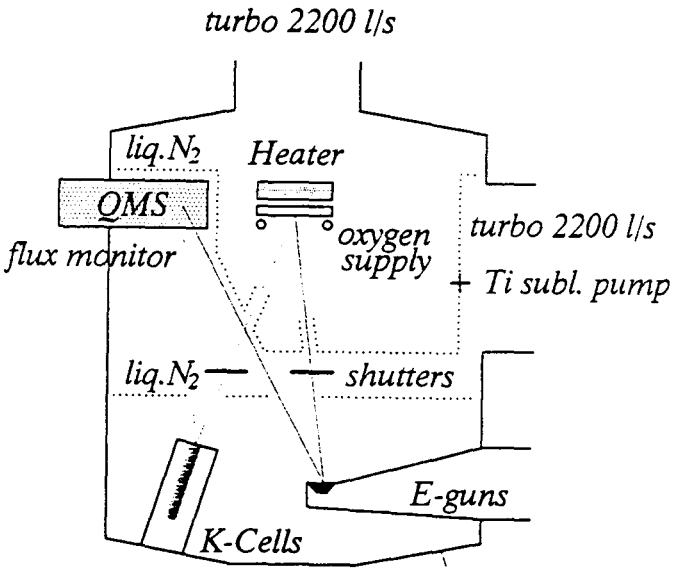

Figure 24. Schematic drawing of the oxi-MBE system.

The MBE system is build around an ultra high vacuum chamber. In this apparatus two types of sources are installed: e-guns, where atoms of a material (Fe, Ni or Co) are evaporated from the source by electron bombardment and Knüdsen cells, where atoms of a material (Mg, Mn or Cu) are evaporated from the source by heating the material. The

flux of atoms is measured by a quadrupole mass spectrometer (QMS). The sources are separated from the chamber by shutters. The substrate is mounted in the chamber. Through a pipe in the chamber a beam of atoms is created towards the substrate. In order to deposit oxidic materials a ring-shaped oxygen supplier is mounted close to the substrate. The atoms will react with the oxygen at the substrate forming a thin oxidic layer. The used substrate temperature is 525 K during growth and the growth rate is about 0.2 to 0.5 Å/s. Depending on the oxygen pressure, different phases with different oxygen content (such as Fe, Fe_3O_4 and Fe_2O_3) can be formed.
A movable shutter is present close to the substrate. By redrawing this shutter slowly over the substrate during deposition a wedge-shaped layer can be grown. For more detailed information see ref. [23].

4.1.2 XRD and STM.

X-ray Diffraction (XRD) is a method to determine the structure of a material. The sample is exposed to X-rays emitted by a Cu source (λ=1.541838 Å) at an angle θ. The X-rays are reflected by the sample and detected at an angle 2θ with the incoming X-ray beam (Figure 25). The X-rays reflected at different crystal planes, at different layer interfaces and at the bottom and top of the sample interfere constructively if they match the conditions of the Bragg law, given by

$$2d\sin(\theta) = n\lambda \quad (n = 1,2,3,\ldots) \qquad (23)$$

where d is the distance between subsequent crystal planes or the top and bottom of the sample. Constructive interference shows up as a peak in the intensities of the reflected beam in a scan over the detected angles. The acquired scan of the interference pattern gives information about the crystal orientation, perpendicular lattice constants, multilayer period and the thickness of a sample.

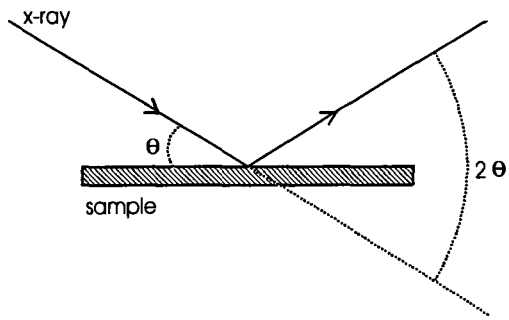

Figure 25. X-ray diffraction geometry.

Scanning Tunnelling Microscopy (STM) is a method to investigate the surface structure of a material. A very fine, atomically sharp, tip is brought close to the surface of a material. By applying a potential, electrons can tunnel between the surface and the tip. The tunnelling current will depend on the ion density of states at the surface. By scanning the surface, an image of the surface structure can be obtained.

4.2 Magnetic characterisation.

4.2.1 Magneto Optical Kerr Effect.

When polarised light is reflected by the surface of a magnetic material, the polarisation of the light beam is changed depending on the magnetisation of the material. This is the so called Magneto Optical Kerr Effect (MOKE) first reported in 1877 [24]. The Kerr effect is a result of the appearance of a magneto optical parameter in the permittivity. An extensive mathematical treatment of the magneto optical effects in terms of the Fresnel parameters can be found in refs. [25, 26].
Linearly polarised light consists of an equal amount of left and right circularly polarised light with the same phase. When reflected by a magnetised surface the ratio between the amplitude of the left and right components and their relative phase will change. The reflected light beam will be elliptically polarised. The change in amplitude is defined as the ellipticity (ε_K) and the change in relative phase is defined as the rotation (θ_K), see (Figure 26).

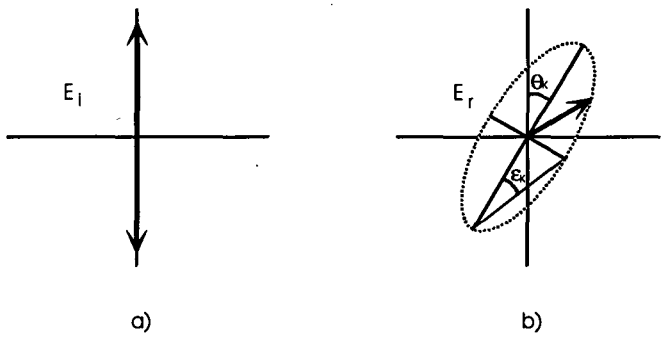

Figure 26. a) linearly polarised light, incident (E_i) and b) elliptically polarised light, reflected (E_r). ε_K represents the ellipticity and θ_K the rotation.

The amount of ellipticity and rotation is proportional to the magnetisation of the material in the direction of the incoming light. Two different geometries of the incident light to the magnetisation are used: polar, where the incident light beam and measured magnetisation is perpendicular to the film plane and longitudinal, where the light beam is at an angle of about 45° to the normal of the film plane (Figure 27).

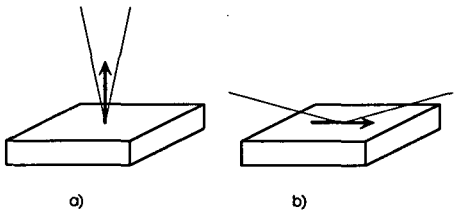

Figure 27. The two different geometries used a) polar, b) longitudinal Kerr effect.

The polar Kerr effect can be described in terms of a circular basis [26]. In this basis the light is considered to be a superposition of right circularly polarised light and left

circularly polarised light. The Jones matrix for reflection in the polar geometry on the circular basis is given by

$$R_{\pm} = \begin{pmatrix} r_{+}e^{i\delta_{+}} & 0 \\ 0 & r_{-}e^{i\delta_{-}} \end{pmatrix} \tag{24}$$

where the subscripts + and - represent right and left circularly polarised light respectively. $r_{\pm}$ represents the amplitude and $\delta_{\pm}$ represents the phase of the reflected light. The Kerr angles are defined as

$$\theta_K = \frac{1}{2}(\delta_{+} - \delta_{-}) \tag{25}$$

$$\varepsilon_K \approx \frac{r_{+} - r_{-}}{r_{+} + r_{-}} \tag{26}$$

where the last expression is an approximation for the case of $r_+ \approx r_-$. From these expressions it is clear that the ellipticity only depends on the relative change of amplitude of the components while the rotation only depends on the relative phase shift.
To describe the Kerr effect for the longitudinal situation the circular basis can not be applied so that a different basis, the senkrecht and parallel basis (sp-basis), will be used. Senkrecht means the direction of the light perpendicular to the plane of incidence and parallel means the direction in the plane of incidence of the light. The Jones matrix for reflection on the sp-basis is given by

$$R_{s/p} = \begin{pmatrix} r_{ss}e^{i\delta_{ss}} & r_{sp}e^{i\delta_{sp}} \\ -r_{sp}e^{i\delta_{sp}} & r_{pp}e^{i\delta_{pp}} \end{pmatrix} \tag{27}$$

The amplitude and phase changes for the longitudinal effect are related to the optical properties [27]. The component $r_{sp}e^{i\delta_{sp}}$ is proportional to the off-diagonal part of the relative permittivity tensor. The tensor depends linearly on the magnetisation. The expressions for θ_K and ε_K, derived under the assumption that $r_{sp} \ll r_{ss}$, are

$$\theta_K \approx \frac{r_{sp}}{r_{ss}}\cos(\delta_{ss} - \delta_{sp}) \tag{28}$$

$$\varepsilon_K \approx \frac{r_{sp}}{r_{ss}}\sin(\delta_{ss} - \delta_{sp}) \tag{29}$$

Note that in the sp basis both Kerr angles depend on the phase as well as the amplitude differences.
The actual ellipticity and rotation depends on the wavelength of the light used and its penetration depth. Using a focused light beam makes it possible to measure the magnetisation locally on the sample by means of MOKE. The main advantage of measuring the magnetisation locally on a sample is the possibility of using wedge shaped samples. Using wedge shaped samples provides a fast and easy way to measure magnetisation of a certain combination of layers at different thicknesses of the layers. A

disadvantage of MOKE is that the ellipticity and rotation are proportional to the magnetisation but no quantitative information about the magnetisation can be determined. Figure 28 gives a schematic diagram of the MOKE set-up used. As a light source a He-Ne laser, λ = 633 nm, is used. The beam passes through a diaphragm to inhibit reflection back into the laser by other parts of the set-up. After the diaphragm the light is polarised by a polariser. The following element is a Photo Elastic Multiplier (PEM). The PEM consists of a vibrating optical crystal (f = 20-50 MHz). When the polarisation angle of the light is at an angle of 45° to the vibrating axis of the crystal, the polarised light shining through the crystal is transformed in alternating left and right circularly polarised light. An explanation of this measurement technique is given in refs. [28,29].
The light then passes a lens to focus the beam onto the sample. After reflection the light passes an analyser. Only the component of the light along the polarisation direction of the analyser is transmitted. In the case of zero ellipticity, the intensity of the transmitted light is constant, otherwise the intensity of the transmitted light will be modulated by f for ellipticity and 2f for rotation. After the analyser, a photodiode is used to measure the lights intensity. A lock-in amplifier is used to process the modulated signal. Using a modulating signal improves the signal to noise ratio and distinguishes the ellipticity from the rotation.
The sample is mounted on a manipulator consisting of two x/y tables both equipped with a steppermotor. By means of this manipulator the position of the laser beam on the sample can be changed with this manipulator, which enables a scan along the sample. To vary the magnetic field applied to the sample a water cooled electromagnet is used. The field is measured using a Hall probe mounted on one of the magnet cores. The whole system, including the data acquisition, is computer controlled.
The system described here is the longitudinal MOKE set-up where the applied field is in plane of the sample. With minor adjustments the longitudinal set-up can be changed to the polar Kerr set-up, where the field is perpendicular to the sample.

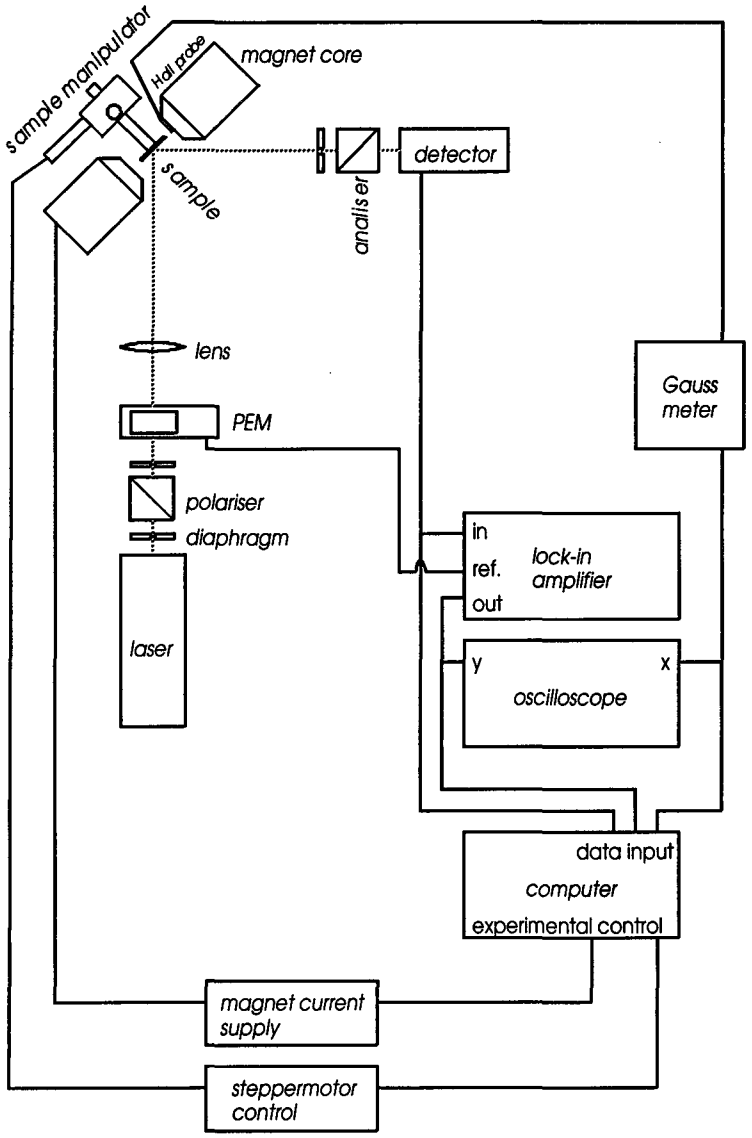

Figure 28. Schematic diagram of the MOKE equipment.

4.2.2 SQUID

A Superconducting QUantum Interference Device (SQUID) magnetometer (Quantum Design MPMS5) is a very accurate tool to measure the magnetisation of a sample [30]. In the SQUID magnetometer the magnetic sample is moved through a set of superconducting coils. The flux through the coils is measured as a function of the position of the sample. From the acquired data the magnetisation of the sample can be calculated by fitting a magnetic dipole response. To be able to measure the magnetisation as a function of the applied magnetic field a superconducting electromagnet is also available in the SQUID magnetometer. The field is maximal 5 T. The temperature range for the

measurements is 1.7 K to 400 K. The SQUID is sensitive to magnetisations of about 10^{-5} emu. With a SQUID the total magnetisation of the sample is measured.

4.3 Interpretation of the hysteresis loops.

4.3.1 Anisotropy.

In a magnetic material, the directions of the spins are not all equivalent: one ore more directions are preferred over other directions. This phenomenon is called anisotropy [31]. The preferred direction of the magnetisation is called the easy axis, the least preferred direction of the magnetisation is called the hard axis.
The anisotropy may be separated into four contributions determining the overall anisotropy: shape, magnetocrystalline and magnetoelastic. The shape anisotropy is due to the demagnetisation energy caused by the magnetic field produced by the material itself. Magnetocrystalline anisotropy is due to the spin orbit coupling and will tend to align the magnetisation along one of the symmetry axes of the crystal. Magnetoelastic anisotropy arises from changes of the crystal structure due to strain in the material.

4.3.2 The hysteresis loops.

A hysteresis loop is a graph of the magnetisation, or a related quantity such as ellipticity, versus the applied magnetic field and is measured by sweeping the applied field from positive to negative and back.
In Figure 29 this process is depicted for a single domain film. As an example consider a system with in plane preferred magnetisation and a four fold anisotropy. At zero field the magnetisation will be along one of the easy axis. The field is applied along an in plane hard axis. Recall that by MOKE or SQUID the component of the magnetisation in the direction of the applied field is measured. When a sufficiently large field is applied the magnetisation will saturate along the applied field (Figure 29a). When decreasing the applied field the magnetisation will rotate towards one of the easy axis (Figure 29b). Note that the magnetisation can also rotate towards the other easy axis. At zero field the magnetisation will be along the easy axis (Figure 29c). The remaining magnetisation at zero field in the measured direction is called the remanence, usually expressed as a ratio to the saturation magnetisation. When the applied field is decreased further (Figure 29d) at a certain field (the coercive field) the magnetisation will flip to an energetically more favourable easy axis (Figure 29e). The coercive field is a result of the anisotropy forces in the material. Decreasing the applied field will rotate the magnetisation towards the field (Figure 29f) and the magnetisation will saturate along the field again (Figure 29g). Figure 29h shows the measured hysteresis loop. In the example given the remanence will be 70% because the applied field is at an angle of 45° to the easy axis, thus the projection of the magnetisation, at zero field, along the direction of the applied field is $1/2\sqrt{2}M$. When the applied field is along the easy axis the remanence will be 100% and a square hysteresis loop will be measured.

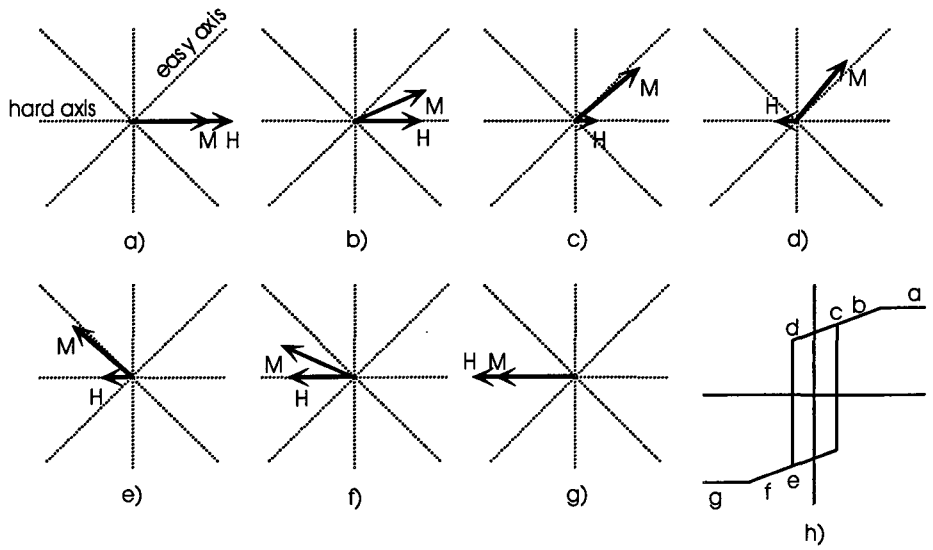

Figure 29. Change of the orientation of the magnetisation, M, as a function of the applied magnetic field, H.

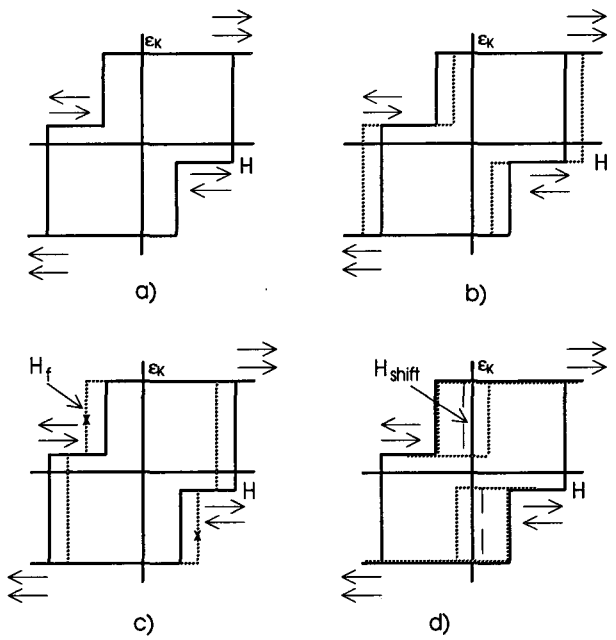

Figure 30. Hysteresis loops in a coupling experiment. a) ferromagnetic coupled system, b) antiferromagnetic coupled system. c),d) loops to explain determination of the coupling strength: c) direct, d) via inner loop measurement. The arrows represent the direction of the magnetisation of the different magnetic layers.

In case of interlayer coupling experiments loops such as depicted in Figure 30 are measured. The loops consist of the contributions of the two separate magnetic layers, one with a larger coercive field and magnetic moment and one with a smaller coercive field and magnetic moment. Figure 30a shows a loop in the absence of magnetic coupling and the field applied along the easy axis. Starting at the top right the magnetisation of both layers has the same direction. The measured magnetisation is the superposition of the magnetisation of both layers. When the applied field is decreased, at a certain point the magnetisation of the soft magnetic layer (with the lowest magnetic moment) flips. The magnetisation of both layers now is in an opposite direction. After decreasing the field further the second layer will also flip and both layers will have the same direction again.
Figure 30b shows two weakly antiferromagnetic coupled layers. At sufficiently large fields the magnetisation of both layers will be in the same direction. Decreasing the field will make the layer with the lower coercive field and magnetic moment flip because it favours an antiparallel orientation to the layer with the larger magnetic moment. In the case depicted in Figure 30b the layer with the small magnetic moment also has the small coercive field. After decreasing the field further the second layer will also flip and both layers will have the same direction again.
In case of weak ferromagnetic coupling the layers tend to be parallel oriented. The magnetisation of the soft magnetic layer will flip later and the magnetisation of the hard magnetic layer will flip earlier, indicated by the dotted line in Figure 30c. When the layers are strong ferromagnetic coupled the layers will behave as one magnetic entity with a coercive field in between the coercive fields of the separate layers and the separate contributions can not be distinguished. The field at which the magnetisation flips, when coupling is present, is called the flip field, H_f. The flip fields of the different layers will shift towards each other as the ferromagnetic coupling strength increases. When the hysteresis loop from which the values for H_f and H_c are determined are measured along the easy axis, equations for the coupling strength, J, can be derived by equating the coupling energy (J/t) and the Zeeman energy density of the hysteresis loop ($\mu_0(H_f-H_c)dM$) [32]. The expressions for J are

$$J = \left(H_f^{(1)} - H_c^{(1)}\right)\mu_0 M_s^{(1)} t^{(1)} \qquad (30)$$

$$J = \left(H_c^{(2)} - H_f^{(2)}\right)\mu_0 M_s^{(2)} t^{(2)} \qquad (31)$$

where $H_f^{(1)}$, $H_f^{(2)}$ are the flip fields of the layers with small and large coercive field respectively. $H_c^{(1)}$, $H_c^{(2)}$ are the coercive fields of the decoupled layers, $M_s^{(1)}$, $M_s^{(2)}$ are the saturation magnetisations of the two layers and $t_s^{(1)}$, $t_s^{(2)}$ are the thicknesses of the layers. From these equations the flip field of the strong ferromagnetic coupled system can be determined by equating $H_f^{(1,2)} = H_f^{(1)} = H_f^{(2)}$

$$H_f^{(1,2)} = \frac{H_c^{(1)} M_s^{(1)} t^{(1)} + H_c^{(2)} M_s^{(2)} t^{(2)}}{M_s^{(1)} t^{(1)} + M_s^{(2)} t^{(2)}} \qquad (32)$$

An other way to determine the coupling strength is to measure a so-called inner loop (Figure 30d), where the hysteresis loop of the soft magnetic layer is determined

separately. The field is swept from a positive field to a negative field where the magnetic hard layer has not flipped yet. When the field is increased again only the behaviour of the magnetic soft layer is measured, indicated by the dotted line in Figure 30d. The procedure is repeated coming from a large negative field. If coupling is present the inner loops will be shifted relative to each other. The shift is a measure for the coupling strength. This method of determining the coupling strength only works if there is a distinct flat plateau between the flip fields of the two magnetic layers. If there is no flat plateau the magnetisation of the soft layer is not saturated or the magnetisation of the hard layer already starts to flip, so that the determination of the coupling strength from the inner loop can not be made.

5. Interlayer coupling of two magnetite layers across different spacers.

In this chapter the results of the measurements are presented and discussed. The general composition of the samples is outlined in the first paragraph. The second paragraph discusses the substrates that were used. Next the results of the characterisation of the Fe_3O_4 surface will be presented. The remainder of the chapter is about the results of the measurements on interlayer coupling between two magnetite layers across Cu, MgO, Mn_3O_4 and CoO.

5.1 Composition and structure of the samples.

5.1.1 General composition.

The basic structure consisted of two magnetite layers separated by an interlayer (MgO, CoO, etc.). In some experiments the bottom magnetite layers was grown on top of a $Co_xFe_{3-x}O_4$ baselayer in order to slightly modify the magnetic properties of the bottom magnetite layer in comparison to the top magnetite layer, thus rendering the magnetite layers distinguishable, see next paragraph. Two types of sample structures were studied: wedge shaped structures, where the $Co_xFe_{3-x}O_4$ and Fe_3O_4 layers were deposited with uniform thickness and the spacer was deposited in the form of a wedge and uniform structures, where all layers had a uniform thickness. A schematic representation of the samples is shown in Figure 31.

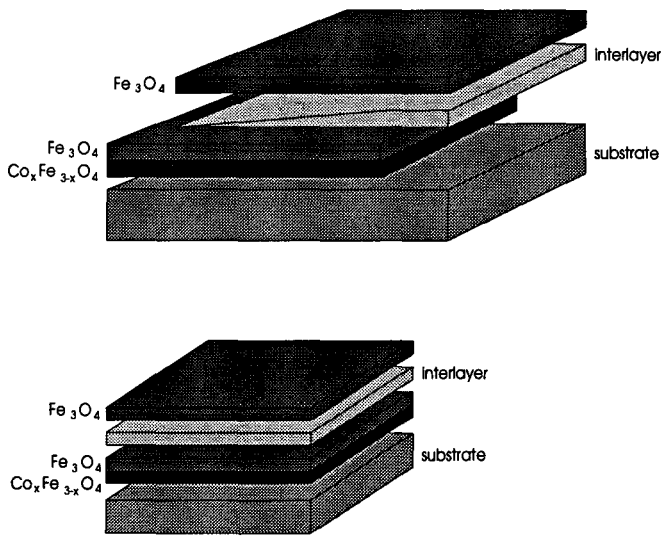

Figure 31. Schematic representation of the samples. A wedge shaped sample used in MOKE experiments (top) and a uniform sample used for SQUID experiments (bottom) are shown.

The wedge shaped samples were investigated by MOKE magnetometry, while the uniform samples were investigated by means of SQUID magnetometry. During the MOKE experiments a laser is scanned along the wedge, which makes it possible to measure the coupling between the magnetite layers as a function of the spacer thickness. Note that an additional advantage of the wedge shaped samples is that on one sample all thicknesses are grown under identical circumstances. The structure of the wedge shaped samples is grown with the wedge and top magnetite layer shifted with respect to the bottom bilayer, which enables the measurement of the magnetic behaviour of the bottom bilayer and the top layer separately.
The SQUID measurements on the uniform samples give information on the exact size of the magnetisation and enables temperature dependent measurements of the magnetisation. Depending on the number of uniform samples used only a limited number of thicknesses can be measured. In order to enhance the signal to noise ratio the stack of layers on the uniform samples can be repeated a few times to increase the quantity of magnetic material and thus the magnetisation of the sample.
Both MOKE and SQUID measurements are used to complement each other thus forming a more complete magnetic picture.

5.1.2 The hard and soft magnetic layer trick.

To be able do distinguish the two magnetite layers magnetically, one of the layers is grown on top of a $Co_xFe_{3-x}O_4$ layer, with x varying between 0.17 and 0.22. Due to strong ferromagnetic coupling at the interface the (Fe_3O_4 / $Co_xFe_{3-x}O_4$) bilayer will act as one magnetic entity. The magnetic properties of the bilayer will be in between the properties of the single materials weighed by the ratio of their magnetic moment (paragraph 2.2.4). $Co_xFe_{3-x}O_4$ has a higher coercivity than Fe_3O_4 so that the bilayer will have a coercive field in between their separate coercive fields. This makes it possible to distinguish the two magnetite layers magnetically by the difference in their coercive fields.

5.2 The substrates used, MgO and $MgAl_2O_4$.

Two kind of substrates have been used: MgO (100) and $MgAl_2O_4$ (100). MgO is used because of its small lattice mismatch with Fe_3O_4. The lattice mismatch is defined as $(a_s-a_f)/a_f$, with a_s, a_f the lattice constants of the substrate and the film, respectively. The lattice mismatch between the oxygen lattice of MgO (100) and the oxygen lattice of Fe_3O_4 (100) is +0.3%. This results in pseudomorphic growth of Fe_3O_4 on MgO up to at least 500 Å (pseudomorphic growth means epitaxial growth, with the lattice of the Fe_3O_4 fully strained to the MgO lattice, so that no dislocations are present at the interface). It has been shown earlier that structural high quality thin Fe_3O_4 films can be grown on MgO (100) with the Oxi-MBE [33]. The lattice mismatch between $MgAl_2O_4$ (100) and Fe_3O_4 (100) is -3.7%, which results in a reduced structural quality of the Fe_3O_4 films grown on $MgAl_2O_4$ then the Fe_3O_4 films grown on MgO [34].
$MgAl_2O_4$ has been used to ensure that the magnetisation of the $Co_xFe_{3-x}O_4$ layer is in plane. The lattice constant of $Co_xFe_{3-x}O_4$ is close to the lattice constant of Fe_3O_4, which results in pseudomorphic growth of $Co_xFe_{3-x}O_4$ on MgO (100). The tensile strain due to

the pseudomorphic growth gives rise to a magnetoelastic contribution to the anisotropy resulting in a perpendicular orientation of the magnetisation of the $Co_xFe_{3-x}O_4$ / Fe_3O_4 bilayer grown on MgO (100). The magnetisation of the top Fe_3O_4 layer is in plane. The combination of these two different orientations would complicate the analysis of the magnetic measurements on the samples. The smaller lattice parameter of $MgAl_2O_4$ in comparison to $Co_xFe_{3-x}O_4$ ensures that the magnetisation of the $Co_xFe_{3-x}O_4$ / Fe_3O_4 bilayer is in plane, therefore $MgAl_2O_4$ has been used as a substrate [31].

5.3 Surface structure of Fe_3O_4.

XRD data and STM measurements of the epitaxial growth of magnetite on MgO (100) by oxidic-MBE are presented in ref. [35]. Figure 32 shows the result of a STM study of a 400 Å thick Fe_3O_4 layer grown on a MgO (100) substrate. Before the STM measurements the surface was cleaned because the sample had to be transported through the air from the MBE apparatus to the STM. First the sample was sputtered with 500 eV Ar ions at room temperature for 15 minutes. This was followed by a temperature ramp of 20 min. to 600° C during which the sputtering continued until the temperature exceeded 500° C. At 600° C the sample was annealed for 30 min., after which it was cooled to room temperature. It is unknown whether this treatment will influence the structure or surface of the Fe_3O_4 significantly.

Figure 32 shows that the Fe_3O_4 surface consists of atomically-flat terraces with a width of about 100 Å to 1000 Å. The bottom part of Figure 32 shows a cross section of the surface, which reveals that the steps between the terraces have a height between 2 Å and 12 Å.

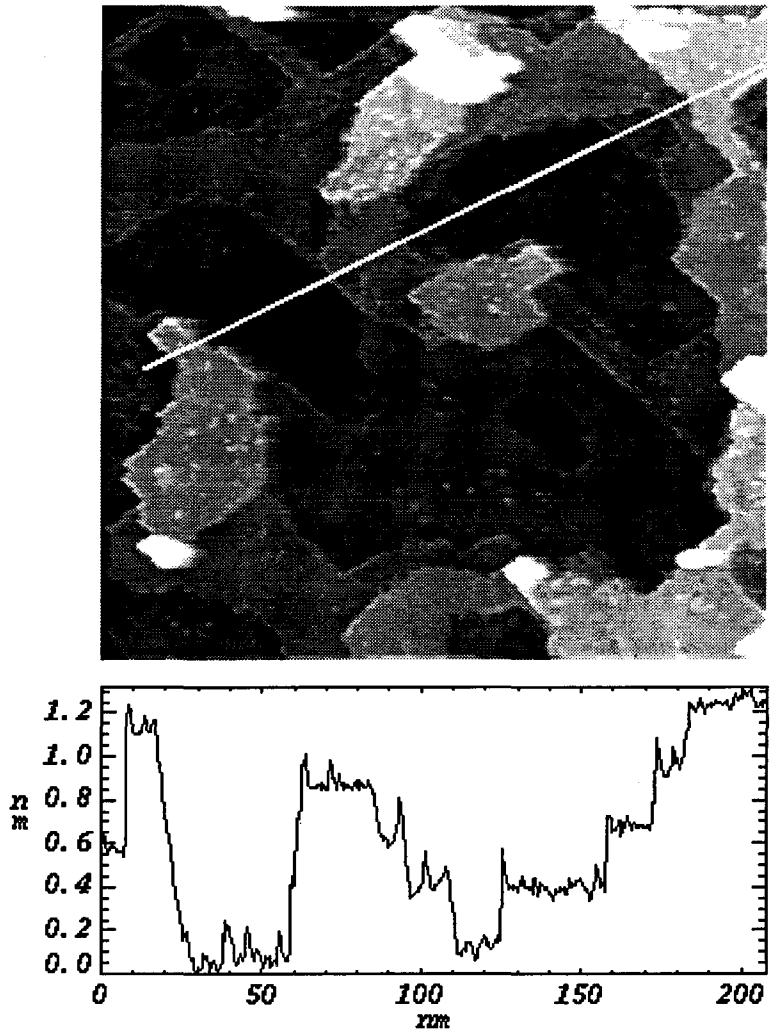

Figure 32. STM measurement of a 400 Å thick Fe_3O_4 layer on grown MgO (100). The graph at the bottom of the figure shows a cross section of the interface along the white line in the upper part of the figure (after [36]).

5.4 Two magnetite layers separated by a non-magnetic MgO spacer.

The interlayer coupling between two magnetite layers across a non-magnetic insulating MgO spacer has been studied. MgO was chosen because it is often used as a tunnel junction and because MgO has a good lattice match to Fe_3O_4. Since Fe_3O_4 is a half metallic conductor and MgO is an insulator the system can be seen as a prototype of two conducting ferrimagnets separated by a non-magnetic insulator, so that coupling between the ferrimagnets might arise from tunnelling of electrons through the insulating spacer (paragraph 2.2.1). The structure of the first investigated sample was: $MgAl_2O_4$ (100) / 325 Å $Co_{0.2}Fe_{2.8}O_4$ / 325 Å Fe_3O_4 / wedge 0-83 Å MgO / 215 Å Fe_3O_4.

The magnetic properties were measured with MOKE in the longitudinal geometry with the field applied along the (110) direction (easy axis). Both single hysteresis loops

(without measuring the inner loop) as well as multiple loops (with measurement of the inner loop) were measured (Figure 33). These hysteresis loops show that below 6.5 Å of MgO a single 100 % remanent loop is measured indicating strong ferromagnetic coupling between the magnetite layers (Figure 33a). With increasing MgO thickness the coupling decreases rapidly and stepped loops are measured. At thicknesses above 10 Å only a small ferromagnetic coupling remains as can be seen from the relative shift of the inner loops. The small coupling is retained up to 83 Å (Figure 33c,d,e,f).

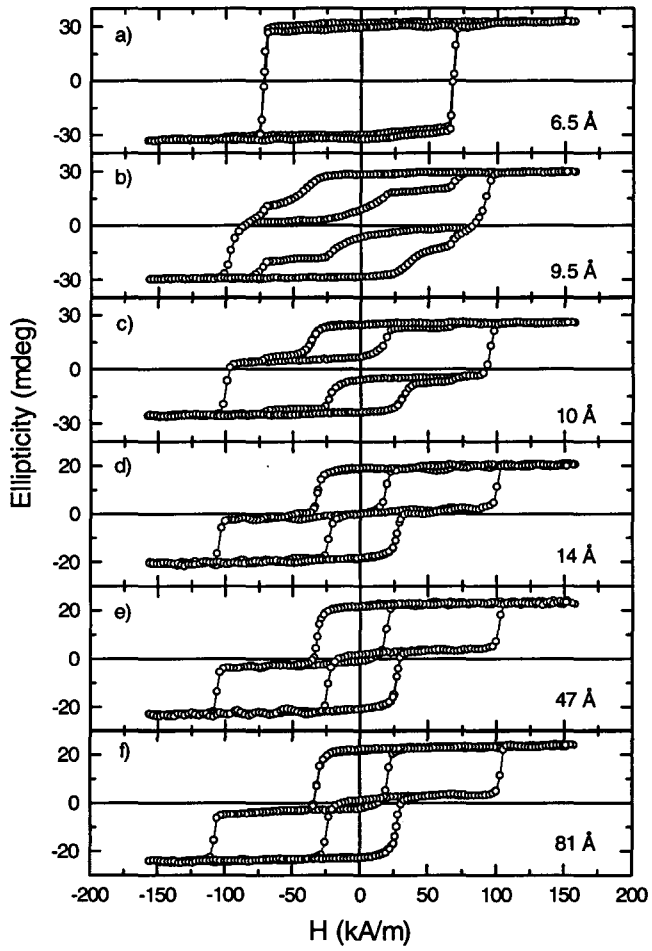

Figure 33. Several hysteresis loops representative for the MOKE measurements on the $MgAl_2O_4$ (100) / $Co_{0.2}Fe_{2.8}O_4$ / Fe_3O_4 / MgO / Fe_3O_4 sample. These loops show the inner loops for the soft magnetic layer.

As described in the previous chapter two ways of calculating the coupling strength are available: from the flip field and from the shift of the inner loops. Since the inner loops can not be measured accurately below 10 Å of MgO, the first method is applied for the thicknesses below 15 Å of MgO. Figure 34 shows the thickness dependence of the flip field for the soft magnetic layer. The flip field of the soft magnetic layer is determined at 1/3 of the saturation ellipticity. The inset in Figure 34 shows the coupling strength calculated from the flip field, using equation (30). The parameters used were: $t^{(1)} = 215$ Å, $\mu_0 M_s = 0.62$ T [17] and $H_c^{(1)} = 18.7$ kA/m.

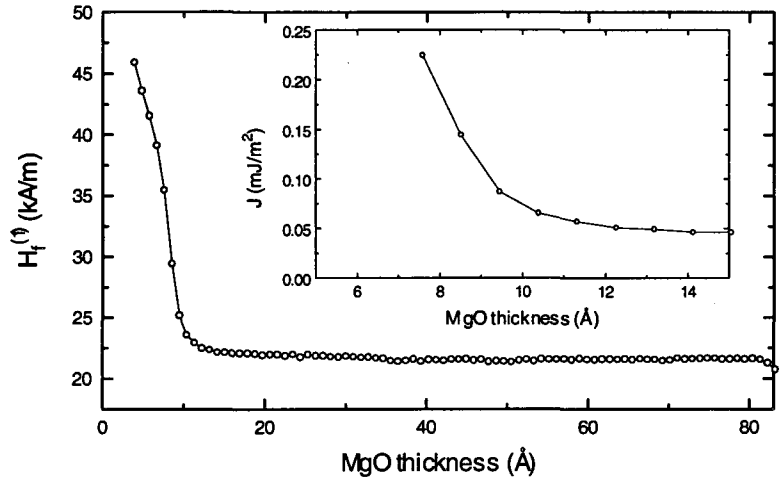

Figure 34. Thickness dependence of the flip field, $H_f^{(1)}$, of the soft magnetic layer and the calculated coupling strength, J. The flip field was determined from hysteresis loops without a inner loop measurement and the coupling strength was calculated using equation (30).

In the appendix an estimate of the sign and strength of the coupling is calculated, based upon the tunnelling theory given in paragraph 2.2.1. This theoretical contemplation yields an antiferromagnetic coupling, which contradicts the observation of a ferromagnetic coupling for this system. The calculations result in a J_0 of 8.1 meV and 2κ of 0.04 $Å^{-1}$. The coupling strength calculated from the measurements can not be fitted using the tunnelling theory (equation (12). Thus tunnelling seems *not* to be the coupling mechanism in this system. However, some remarks have to be made concerning the theoretical estimate. The band structure used does not necessarily have to be valid to the system investigated, because the band structure at the Fe_3O_4 / MgO interface might be different and the effective electron mass is unknown. Furthermore, the theory for tunnelling assumed a metallic system with metallic conductors, not a hopping type conductor like magnetite. Therefore the tunnelling theory might not be applicable to the investigated system.

Alternative coupling mechanisms can be applied to explain the strong ferromagnetic coupling below 10 Å of MgO. An explanation is the existence of pinholes (paragraph 2.2.5). The surface structure of the Fe_3O_4 on MgO (100) revealed by the STM measurements shows terraces of about 200 Å wide with steps up to 12 Å (Figure 32). Although a $MgAl_2O_4$ (100) substrate was used for the coupling sample in stead of a MgO (100) substrate, the surface structure of the Fe_3O_4 is expected to be similar. The observed surface structure shows the possibility of the pinholes below 10 Å of MgO.

Above 10 Å of MgO the flip field gradually, although very slowly, decreases. Figure 33d,e,f show that the inner loops measured are shifted relative to each other, indicating that weak ferromagnetic coupling is present up to, at least, 83 Å of MgO. To be able to determine the coupling strength over a larger MgO thickness interval a new sample was grown with a thicker wedge. The composition was: $MgAl_2O_4$ (100) / 300 Å $Co_{0.2}Fe_{2.8}O_4$ / 300 Å Fe_3O_4 / wedge 20-450 Å MgO / 200 Å Fe_3O_4. This sample was investigated by

means of MOKE magnetometry in the same geometry as the previous sample. The results for the observed field shift and calculated coupling strength are shown in Figure 35.
We ascribe this coupling to 'orange peel' coupling, which is ferromagnetic in case of positively correlated interface roughness (paragraph 2.2.3). The data of the coupling strength was fitted using equation (20), with $\mu_0 M_s$ = 0.62 T. Recall that in the determination of equation (20) a sinusoidal interface roughness was assumed (equation (19)). The result of the fit yields a period, λ, of $(39 \pm 2)\cdot 10^2$ Å and an amplitude, h, of 15.5 ± 0.5 Å (Figure 35). This is consistent with the roughness obtained from the STM data where the average terrace width is approximately 200 Å and the average step height 3 Å. The height fluctuation per unit length (30 / 2000 = 0.0015) obtained from the STM data, is in accordance with the height fluctuation per unit length obtained from the fit of the MOKE data (31 / 1950 = 0.016 ± 0.001).

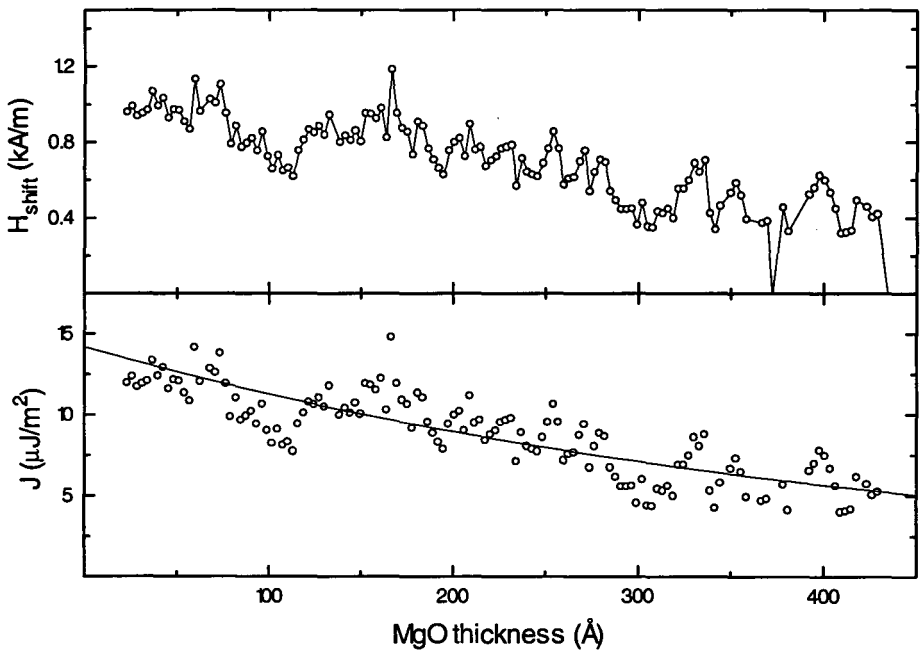

Figure 35. MgO thickness dependence of H_{shift} and the calculated coupling strength (t = 200 Å, $\mu_0 M_s$ = 0.62 T). H_{shift} was determined from an inner loop measurement. The solid line is the fit through the data using equation (20).

5.5 Two magnetite layers separated by a paramagnetic Mn_3O_4 spacer.

To investigate the magnetic coupling between two magnetite layers separated by a paramagnetic material, Mn_3O_4 was chosen as a spacer because Fe_3O_4 and Mn_3O_4 have the spinel structure and like MgO, Mn_3O_4 is an insulator suitable for use as tunnel junction in a spin valve. An additional feature of this system is that the behaviour of the system around the transition temperature of the Mn_3O_4 from paramagnetic to ferrimagnetic can be investigated.

In order to confirm that the Mn_3O_4 is of good structural quality a single film of Mn_3O_4 was grown. The sample structure was $MgAl_2O_4$ (100) / 200 Å MgO / 240 Å Mn_3O_4. High and low angle XRD measurements show that the structure is Mn_3O_4. SQUID magnetometry was used to do the magnetic characterisation (Figure 36). These measurements show bulk magnetic behaviour. The Mn_3O_4 orders ferrimagnetically around 45 K, above 45 K it is paramagnetic (T_C = 24 K [20]) . The magnetic moment is 240 ± 20 kA/m at 10 K close to the literature value of 215 kA/m [20].

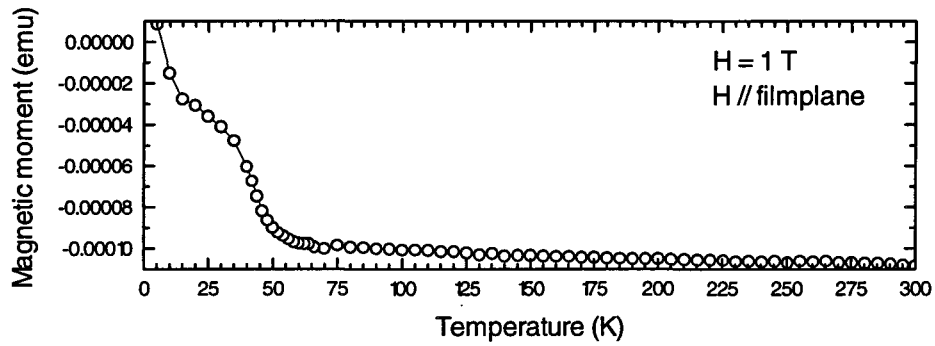

Figure 36. Temperature dependence of the magnetisation of a 240 Å thick Mn_3O_4 film (sample structure: $MgAl_2O_4$ (100) / 200 Å MgO / 240 Å Mn_3O_4). The field was 1 T and applied in the direction of the film plane.

The structure of the studied coupling sample was: $MgAl_2O_4$ (100) / 325 Å $Co_{0.2}Fe_{2.8}O_4$ / 300 Å Fe_3O_4 / wedge 0-65 Å Mn_3O_4 / 200 Å Fe_3O_4.

The magnetic characterisation was done by means of MOKE magnetometry in the longitudinal geometry with the applied field along the (110) direction of the sample. The hysteresis loops were measured with and without inner loops. Examples of the loops with inner loop measurement are shown in Figure 37. These measurements show ferromagnetic coupling up to 65 Å of Mn_3O_4 (end of the wedge). Above 50 Å of Mn_3O_4 a small ferromagnetic coupling is present and below 50 Å of Mn_3O_4 the measurements show a rapidly increasing coupling until below 33 Å Mn_3O_4 only single square hysteresis loops are measured.

From the hysteresis loops without inner loops the flip field of both the soft and hard magnetic layer were determined at 1/4 of the saturation ellipticity (Figure 38). From these data the coupling strength is calculated using equation (30), with $H_c^{(1)}$ = 20 kA/m, $t^{(1)}$ = 200 Å and M_s = 479 kA/m. The theory for calculating the coupling strength from the shift

of the flip field determined from stepped loops breaks down if the loops are not stepped anymore. This means that the values for J below 33 Å (indicated by the dotted vertical line in Figure 38) are an underestimation for the true coupling strength. Hence only a minimum value for the coupling strength of 0.17 mJ/m^2 can be obtained from these data. The coupling strength is of the same order as the coupling strength observed with coupling across MgO.

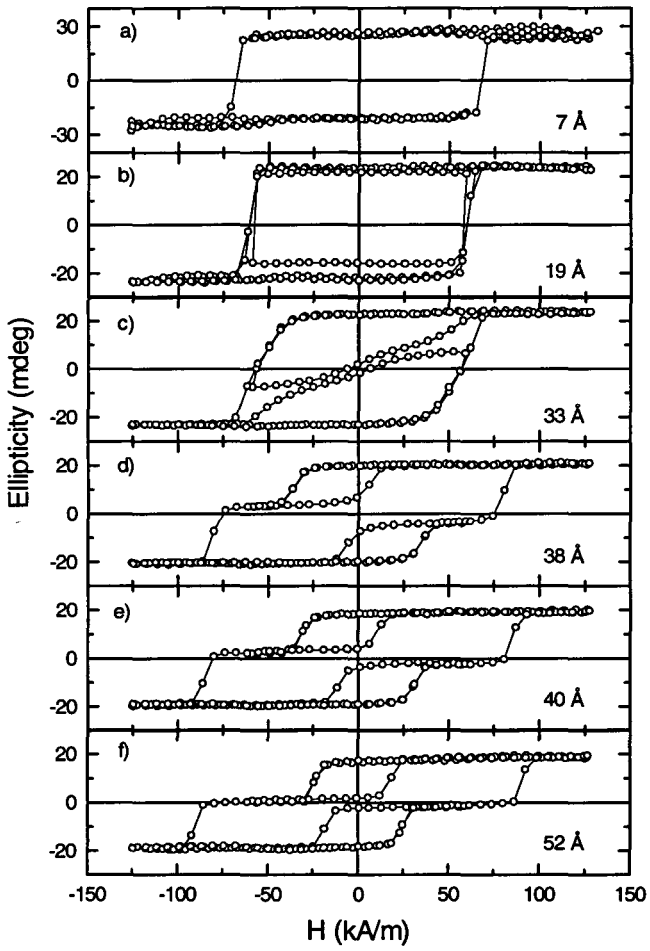

Figure 37. Several representative hysteresis loops measured by means of MOKE on the $MgAl_2O_4$ (100) / $Co_{0.2}Fe_{2.8}O_4$ / Fe_3O_4 / Mn_3O_4 / Fe_3O_4 sample at various thicknesses of Mn_3O_4.

At zero Mn_3O_4 thickness the coercive field of the strong ferromagnetic coupled system is approximately 65 kA/m. Calculation of the flip field at zero Mn_3O_4 thickness by equation (32) yields 66 kA/m (using $H_c^{(2)}$ = 82 kA/m, $t^{(2)}$ = 625 Å and M_s = 497 kA/m for both layers). Thus the measurement is supported by the theory. The decrease in the coercive field of the square hysteresis loops with increasing Mn_3O_4 thickness can be attributed to the Mn_3O_4 between the magnetic layers. The Mn_3O_4 probably has a small coercive field, which decreases the coercive field of the coupled $Co_{0.2}Fe_{2.8}O_4$ / Fe_3O_4 / Mn_3O_4 / Fe_3O_4 stack. The magnetic moment of the Mn_3O_4 is only 5% of the magnetic moment of the

other layers, which does not explain a decrease in the coercive field from 65 kA/m to 55 kA/m. An additional explanation might be that the Mn_3O_4 forms a domain wall nucleation point lowering the coercive field of the stack.

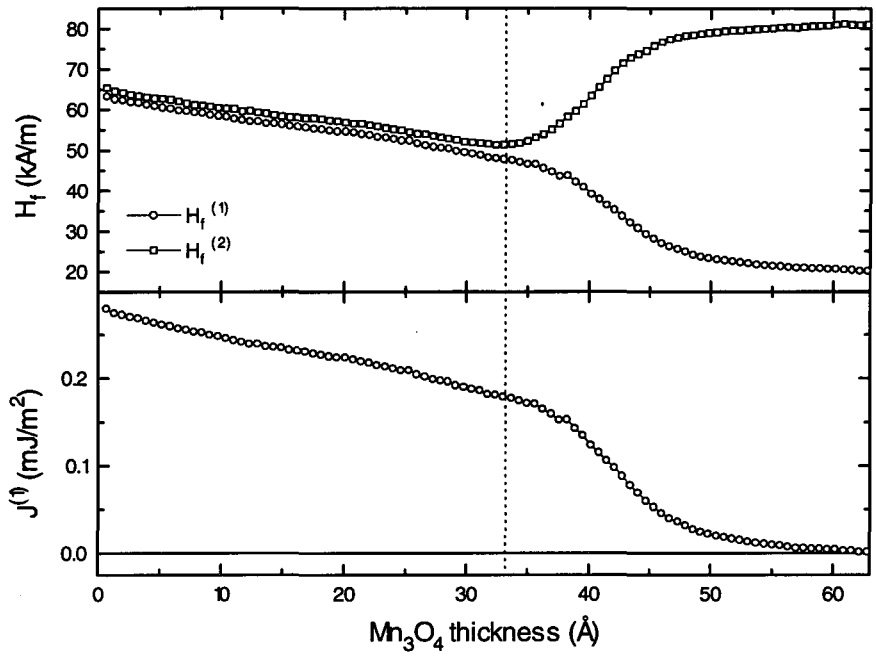

Figure 38. Mn_3O_4 thickness dependence of the measured spin flip field of the top, $H_f^{(1)}$, and bottom, $H_f^{(2)}$, layers (sample structure $MgAl_2O_4$ (100) / $Co_{0.2}Fe_{2.8}O_4$ / Fe_3O_4 / Mn_3O_4 / Fe_3O_4). The coupling strength was calculated from $H_f^{(1)}$, using $H_c^{(1)}$ = 20 kA/m , $t^{(1)}$ = 200 Å and $\mu_0 M_s$ = 0.62 T.

At large thicknesses, above 50 Å of Mn_3O_4, the coupling is ascribed to 'orange peel' coupling, in analogy with the system with a MgO spacer. No additional experiments were performed to confirm this assumption.

The previous experiments with a similar sample structure but MgO as a spacer showed pinholes up to 10 Å of MgO. Since the structural quality and interface roughness for the experiments with a Mn_3O_4 spacer is not different than with a MgO spacer, the strong ferromagnetic coupling up to a Mn_3O_4 thickness of 50 Å is not due to pinholes. Tunnelling is also not likely to give rise to ferromagnetic coupling up to 50 Å because of the stronger than exponential decay of the coupling strength with the spacer thickness (equation (12)). The most probable explanation of the strong ferromagnetic coupling below 50 Å of Mn_3O_4 seems to be proximity magnetism, where the Fe_3O_4 induces a magnetic ordering in the paramagnetic Mn_3O_4 (paragraph 2.2.4).

To investigate the temperature dependence of the coupling several uniform samples were grown with different Mn_3O_4 thicknesses. The general composition was: $MgAl_2O_4$ (100) / M_1 / x Å Mn_3O_4 / M_2 / x Å Mn_3O_4 / M_1 / x Å Mn_3O_4 / M_2, where M_1 = 100 Å Fe_3O_4 / 300 Å $Co_{0.2}Fe_{2.8}O_4$ / 100 Å Fe_3O_4 and M_2 = 200 Å Fe_3O_4. Three samples were grown with a Mn_3O_4 thickness (x)of: 47 Å, 67 Å and 79 Å. The stack is chosen in this order to ensure that the three Mn_3O_4 layers have the same neighbouring layers. The samples were

magnetically characterised using SQUID magnetometry. The hysteresis loops of the 47 Å thick sample measured at different temperatures are shown in Figure 39.

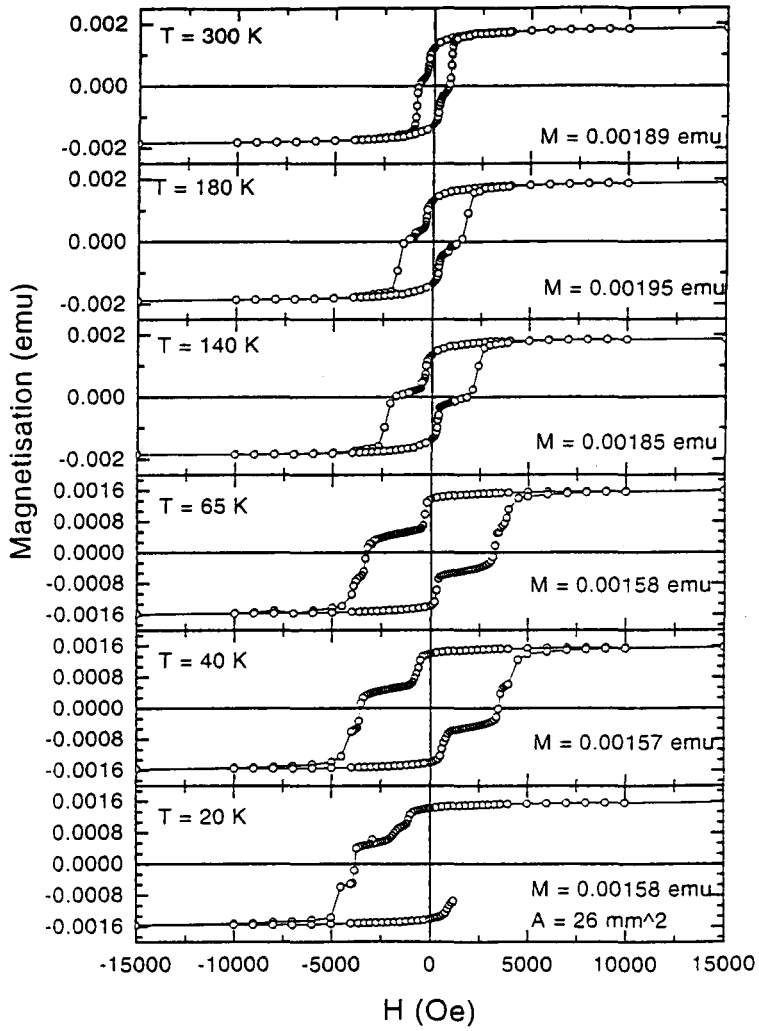

Figure 39. Hysteresis loops measured at different temperatures on a uniform sample with a spacer thickness of 47 Å Mn_3O_4. The saturation magnetisation, M, is indicated in the plots.

In the case of proximity magnetism the thickness of the spacer at which magnetic ordering occurs, is expected to increase with decreasing temperature. Thus the critical thickness of the Mn_3O_4 layer at which strong ferromagnetic coupling between the Fe_3O_4 layers occurs should increase with decreasing temperature. In the absence of proximity magnetism the Mn_3O_4 orders at the Neél temperature (42 K for Mn_3O_4). The flip field of the soft magnetic layer is plotted in Figure 40. To these data the flip field dependence on the temperature of a coupling sample with 50 Å MgO in stead of Mn_3O_4 is added (sample structure: $MgAl_2O_4$ (100) / 300 Å $Co_{0.2}Fe_{2.8}O_4$ / 300 Å Fe_3O_4 / 50 Å MgO / 200 Å Fe_3O_4). The flip field of the Mn_3O_4 samples abruptly increases at 65 K. The MgO sample shows that the flip field gradually increases without coupling. Therefore the abrupt increase of H_f indicates coupling due to proximity magnetism at 65 K.

From the hysteresis loops the magnetisation of the samples can be determined. If the Mn_3O_4 orders magnetically this should mean a change in the magnetisation. Unfortunately, in these experiments the contribution of the Mn_3O_4 to the magnetisation of the total sample is approximately 5% (1400 Å of magnetic material with a bulk magnetisation of 496 kA/m and $3 \times 47 = 141$ Å of Mn_3O_4 with a bulk magnetisation of 215 kA/m), which is within the error bars of the SQUID measurements. Hence magnetisation data do not give the information sought on the ordering of the Mn_3O_4.
The loops in Figure 39 show that the flip field (or coercive field) of the hard magnetic layer increases gradually, probably due to imperfections in the material. Below 65 K a second step appears in the hysteresis loops at the flip field of the hard magnetic layer. This second step can be contributed to the difference between the magnetic hard layer *in* the stack and the magnetic hard layer at the *outside* of the stack. The difference is that the layer in the stack is coupled at two sides while the layer at the outside is only coupled at one side, so that the first layer experiences two times the coupling to the soft layer and the second layer only once. Strangely the flip field of the soft magnetic layer does not show an additional step. Calculating the coupling strength (at 20 K) from the additional step for the hard magnetic layer yields 2 mJ/m^2 (ΔH = 1010 Oe, M = 0.02 A/m), which is to large. With the same coupling strength the expected flip field for the soft magnetic layer would be about 3000 Oe, which is not observed in the hysteresis loops (Figure 39). So far no explanation can be given for these measurements.

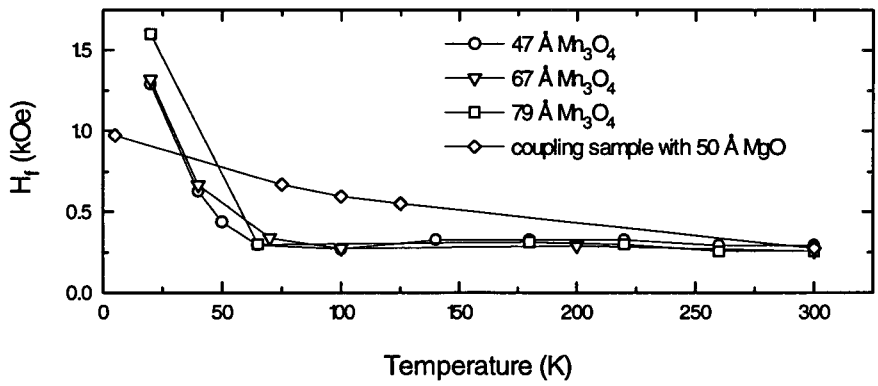

Figure 40. Temperature dependence of the spin flip field of the magnetic soft layer. The data was acquired from SQUID measurements on the uniform samples, for the composition see text.

From the loops in Figure 39 can also be seen that the remanence of the loops increases from approximately 70% to 90% at 65 K, apparently the preferred direction of the magnetisation changes due to the ordering of the Mn_3O_4.
From the SQUID measurements on the uniform samples can be concluded that coupling occurs at 65 K, which could be proximity magnetism because the ordering temperature is increased from 42 K to 65 K. However, the expected thickness dependence of the coupling is not observed because the structures with different Mn_3O_4 thicknesses all order at the same temperature.

5.6 Two magnetite layers separated by a paramagnetic CoO spacer.

Interlayer coupling experiments on two magnetite layers separated by a CoO spacer have been performed. The structure of the sample was: $MgAl_2O_4$ (100) / 300 Å $Co_{0.2}Fe_{2.8}O_4$ / 100 Å Fe_3O_4 / wedge 0-150 Å CoO / 200 Å Fe_3O_4.
The magnetic characterisation of the sample was done by means of MOKE magnetometry in the polar geometry. Several representative hysteresis loops are presented in Figure 41. After analysing the measurements it can be concluded that two different effects are observed, coupling between the magnetite layers and perpendicular magnetisation of the top magnetite layer.

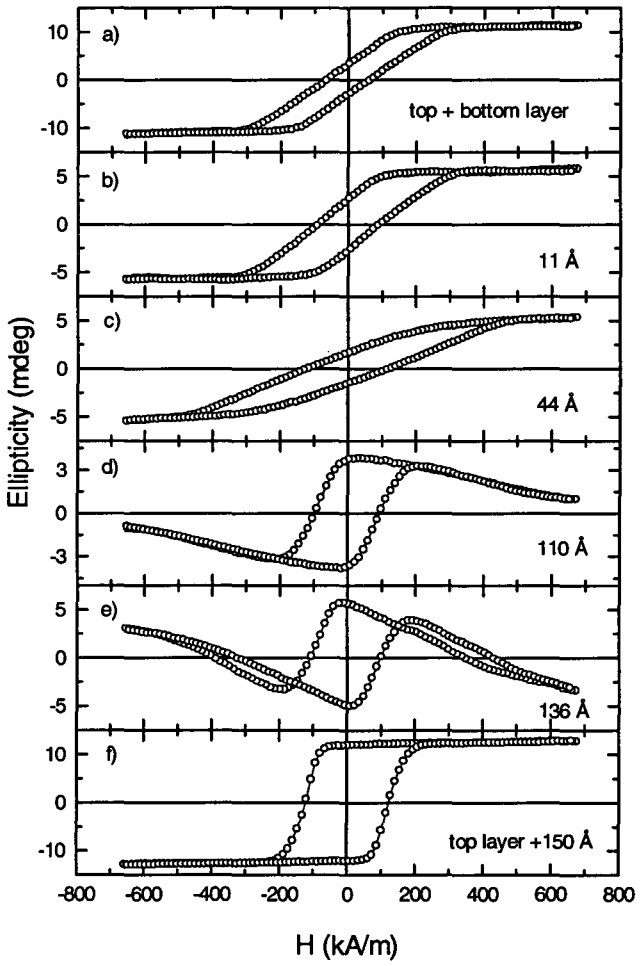

Figure 41. Several hysteresis loops determined with MOKE on the CoO sample (with structure: $MgAl_2O_4$ (100) / $Co_{0.2}Fe_{2.8}O_4$ / Fe_3O_4 / wedge CoO / Fe_3O_4). The loops show the change of preferred magnetisation direction of the top Fe_3O_4 layer.

The polar MOKE measurements on the 200 Å Fe_3O_4 / 150 Å CoO on $MgAl_2O_4$ (100) show a 100 % remanent hysteresis loop (Figure 41f), which indicates a preferential magnetisation direction perpendicular to the film plane. Earlier experiments have shown that due to the strain in a magnetite layer grown on top of a CoO layer the preferred

magnetisation of the magnetite layer changes from in plane to out of plane for a CoO thickness of about 150 Å [31]. Without a CoO baselayer the magnetisation direction of the top Fe_3O_4 layer, as well as the bottom $Co_{0.2}Fe_{2.8}O_4$ / Fe_3O_4 bilayer grown on $MgAl_2O_4$ (100) is in the direction of the plane, which results in loops with low remanence for measurements in the polar MOKE geometry (Figure 41a). Thus the preferred magnetisation direction of the top Fe_3O_4 changes from in plane to out of plane with increasing CoO thickness, while the magnetisation direction of the bottom $Co_{0.2}Fe_{2.8}O_4$ / Fe_3O_4 bilayer stays in plane. The difference in preferred magnetisation direction complicates the analysis of the measurements, so that from the measurements no quantitative information on the coupling constant can be determined. As a result of the difference in preferred magnetisation direction the hysteresis loops will consist of a superposition of a 100 % remanent loop and a loop with low remanence when no coupling is present between the Fe_3O_4 layers. Figure 41d,e show this type of loops, apparently there is no coupling above 100 Å of CoO. Below 50 Å normal single hysteresis loops are measured, which indicates strong coupling between the Fe_3O_4 layers (Figure 41c,d).

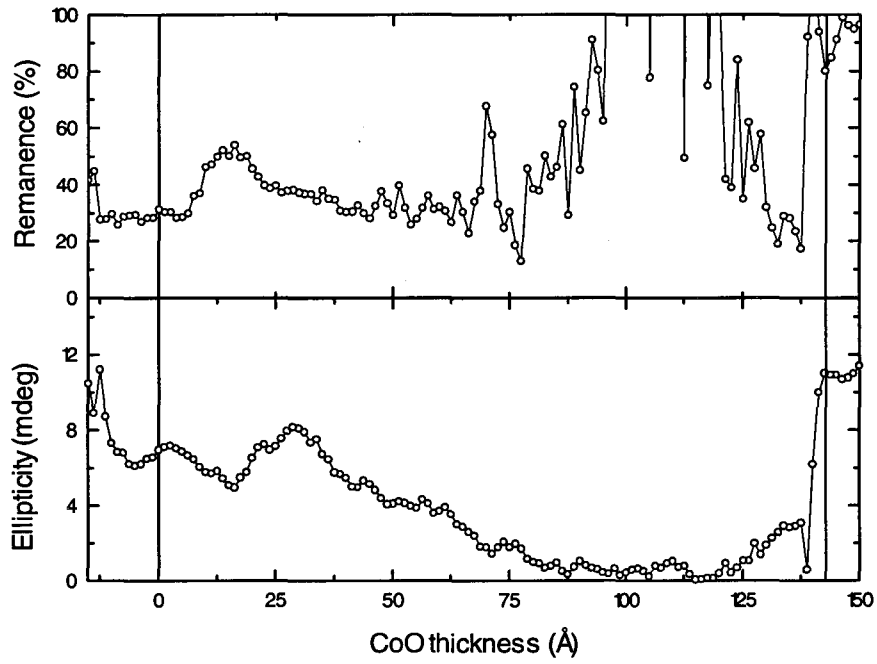

Figure 42. CoO thickness dependence of the remanence and ellipticity for the coupling of two Fe_3O_4 layers separated by CoO. The left of the graph (negative x-axis) is the part of the sample without CoO. The part on the right (above 140 Å CoO) is the part of the sample without the bottom bilayer.

The strange looking shape of the hysteresis loops in the decoupled region is a result of the difference in sign of the ellipticity for the separate contributions to the loops. The magnitude and sign of the ellipticity (and rotation) depends on the wavelength of the light and the composition of the materials. The measured ellipticity is a superposition of the contribution of the individual layers. If the net ellipticity is small the signal to noise ratio of the measurements is small, so that the measured hysteresis loops are of poor quality.

The ellipticity and remanence of the CoO sample are shown in Figure 42. In the region between 50 Å and 125 Å of CoO the measured ellipticity is small. Interpretation of the loops in this region is difficult, which explains the noisy graph of the remanence (Figure 42).
The different sign of the ellipticity of the individual layers leads to the strange looking loops if no coupling is present and leads to a small net ellipticity in case of strong coupling, because the individual contributions destroy each other. Thus it can be concluded from the measurements that below 100 Å of CoO strong coupling is present.
At the CoO thicknesses between 44 Å and 100 Å the magnetisation is difficult to saturate (Figure 41c). The magnetisation of the top Fe_3O_4 layer rotates from out of plane to in plane, as a result of the lower CoO thickness in combination with the coupling to the bottom $Co_{0.2}Fe_{2.8}O_4$ / Fe_3O_4 bilayer.
Neutron diffraction experiments show that for layers of CoO up to 100 Å embedded between Fe_3O_4 the Néel temperature is increased [36]. This increase in Neél temperature indicates that the coupling between the Fe_3O_4 layers is a result of the antiferromagnetism of the CoO layer and the coupling disappears if the CoO becomes a paramagnet.

5.7 Two magnetite layers separated by a metallic Cu spacer.

Previously for metallic systems (Ru wedges between Co and Au) polarisation has been measured [37]. In ref. [37] the observed oscillatory paramagnetic magneto optical Kerr effect, is ascribed to the existence of quantum well states in the Co / Ru / Au. Now a hybrid, oxide / metal / oxide, system is investigated. Quantum well effects are expected to be more pronounced because the metal layer is embedded between two oxides. A sample consisting of two magnetite layers separated by a Cu wedge was grown. The stack consisted of a $MgAl_2O_4$ (100) substrate on which a 200 Å MgO buffer layer, a 300 Å thick Fe_3O_4 layer, a 50 Å to 114 Å Cu wedge and a 200 Å thick Fe_3O_4 layer were grown. The MgO buffer layer was used to improve the crystal quality of the magnetite compared to growth directly on $MgAl_2O_4$. The Cu wedge starts at a thickness of 50 Å to ensure that the Cu layer is continuous (up to 50 Å the Cu grows in the form of islands). Analogue to the Co / Ru / Au system, the Fermi levels of Fe_3O_4 and Cu can be considered as a quantum well system, so that the susceptibility is expected to oscillate with the Cu thickness (paragraph 2.2.2).
The sample was characterised magnetically by MOKE magnetometry. The MOKE experiments were performed in the polar geometry to measure the largest ellipticity response. Figure 43 shows examples of two hysteresis loops.

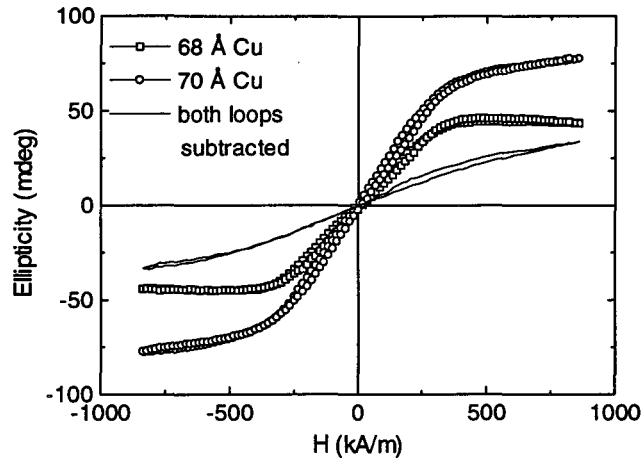

Figure 43. Examples of two hysteresis loops. One at 68 Å without a paramagnetic contribution of the quantum well (smaller slope) and one at 70 Å with a paramagnetic contribution of the quantum well (higher slope). The solid line shows the result if the two loops are subtracted.

The difference between the loop for 68 Å of Cu and the one for 70 Å of Cu is a linear contribution to the second loop, which can be seen by subtracting the loops (Figure 43). This indicates a difference in susceptibility for a Cu thickness of 68 Å and 70 Å.

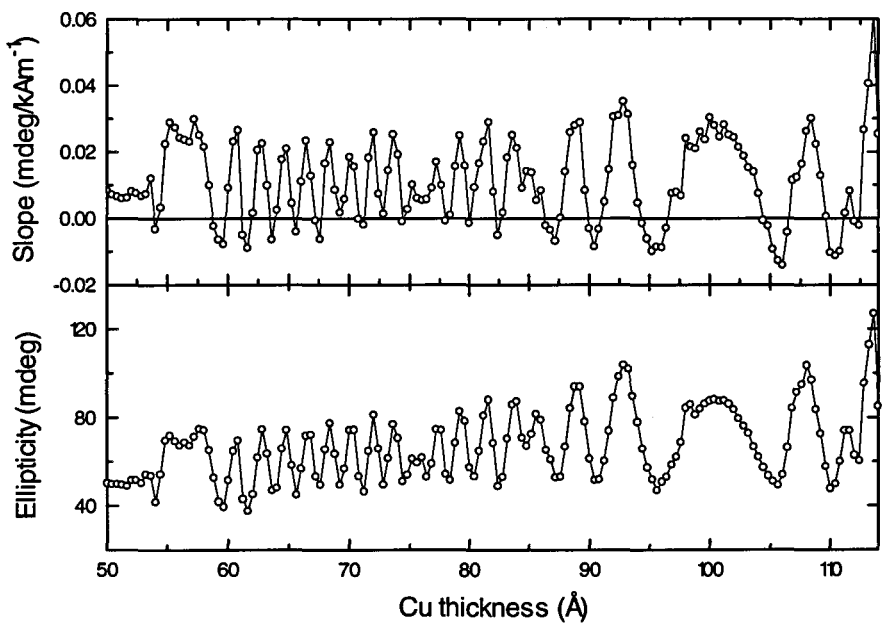

Figure 44. Slope and saturation ellipticity obtained from polar MOKE measurements of a 300 Å Fe_3O_4 layer and a 200 Å Fe_3O_4 layer separated by a 50-114 Å Cu wedge grown on a $MgAl_2O_4$ (100) substrate. The slope of the hysteresis loops is calculated after saturation of the magnetisation of the Fe_3O_4 layers ($|H| > 500$ kA/m).

To be able to determine the contribution of quantum well states to the measured ellipticity (the susceptibility $C\chi^{pauli}B$ in equation (18)), the slope of the hysteresis loops is calculated at the ends of the loop where the magnetisation of the magnetite layers is saturated ($|H| >$ 500 kA/m). The slope and saturation ellipticity obtained are given in Figure 44. From the graph of the Cu thickness dependence of the slope it can be concluded that the ellipticity oscillates with a period of about 2.5 Å. A theoretical calculation predicts a period of 2.3 Å (equation (16), for Cu k_F (100) = $1.36 \cdot 10^8$ cm^{-1} [38]).

To verify this result, a sample with a similar structure was grown on a *different* substrate: MgO (100) / 100 Å MgO / 200 Å Fe_3O_4 / wedge 50-100 Å Cu / 200 Å Fe_3O_4. The results of the slope and saturation ellipticity obtained from polar MOKE measurements are shown in Figure 45. In this second experiment no oscillations in the slope and ellipticity are found.

The results of these two experiments seem to contradict each other. The main difference between the experiments is the use of different substrates: a $MgAl_2O_4$ (100) and a MgO (100) substrate. Therefore the contribution of a blank $MgAl_2O_4$ (100) substrate to the ellipticity is measured. The loops measured showed a straight line of which the slope depended on the position on the substrate (Figure 46). The variation in the measured ellipticity of the $MgAl_2O_4$ substrate is as large as the amplitude of the oscillations measured in the first experiment. This indicates that the oscillations do *not* arise from the Cu spacer, but from the $MgAl_2O_4$ substrate. The substrate contributes to the signal because of the Faraday effect, which is linear with the applied field. The substrate used was polished on both sides, so that the incoming light is reflected not only by the magnetic structure but also by the back of the substrate. This explains that a Faraday contribution of the substrate is present in the ellipticity of the reflected light.

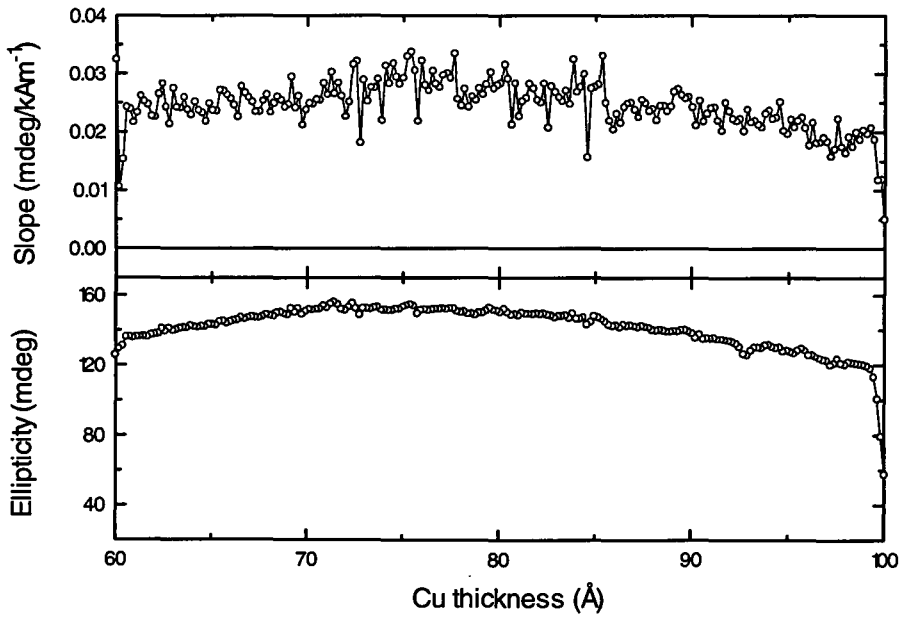

Figure 45. Slope and saturation ellipticity obtained from polar MOKE measurements of two Fe_3O_4 layers separated by a Cu spacer grown on a MgO (100) substrate.

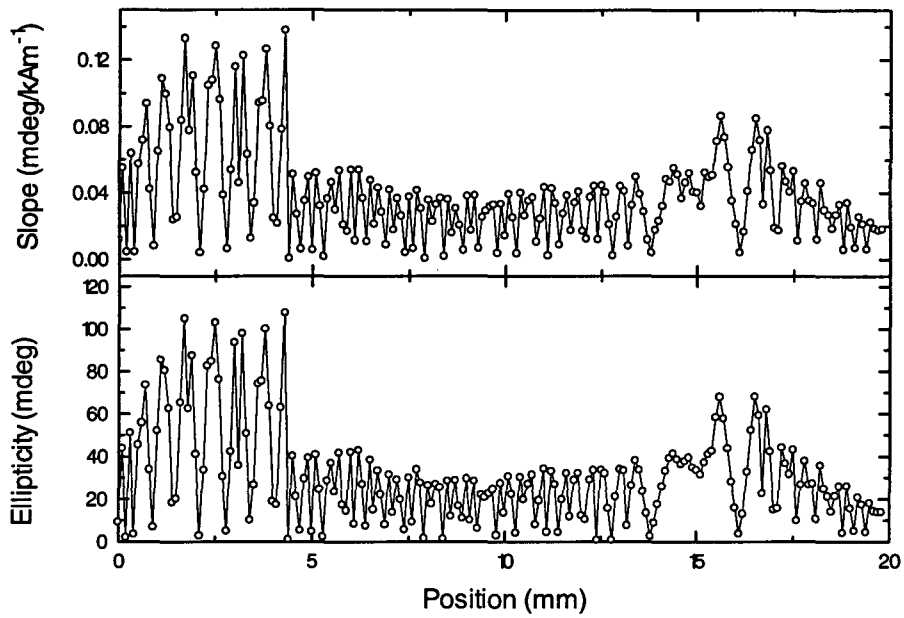

Figure 46. Slope and saturation ellipticity obtained from polar MOKE measurements of the $MgAl_2O_4$ substrate. A scan was made along a blank substrate 20 mm long.

It can be concluded that it has not been possible to observe polarisation in this oxidic / metallic / oxidic system. A possible explanation is that the interfaces between the layers are not sufficiently flat. To observe the oscillations in the susceptibility due to the quantum well states, the boundaries of the well (the Cu / Fe_3O_4 interfaces) have to be sharp. The interface roughness has to be less than the period of the oscillations. The combination of an intrinsic roughness of the Fe_3O_4, with steps larger than the expected polarisation period of 2.3 Å, and roughness due to the expected island like growth of the Cu, explains why the experiment did not work.

6. Conclusions and outlook.

The initial goal of the studies presented in this report was to achieve a system based on two magnetite layers separated by a spacer. The system should be suitable to serve as an oxidic spin valve. Therefore several different insulating materials have been investigated as possible spacer material: nonmagnetic, antiferromagnetic, paramagnetic. To be able to apply a certain material as a spacer, a thickness not larger than about 20 Å is nescessary because the tunneling probability decays exponentially with the thickness of the spacer in a tunnel junction.

For all the materials investigated some form of magnetic coupling has been observed. In general it can be concluded that across an arbitrary oxidic spacer ferromagnetic coupling between two magnetite layers will exist up to about 8 Å as a result of pinholes. These pinholes are due to the interface roughness of the magnetite film. Above a spacer thickness at which pinhole coupling occurs, different spacer materials result in magnetic coupling of different origins:

1) Across a non-magnetic insulating MgO spacer weak ferromagnetic coupling due to 'orange peel' coupling is observed.

2) The use of a Mn_3O_4 spacer resulted in strong ferromagnetic coupling below 55 Å of Mn_3O_4, which is ascribed to proximity magnetism. Above 55 Å of Mn_3O_4 weak ferromagnetic coupling due to 'orange peel' coupling was observed. Bulk Mn_3O_4 is ferromagnetic below and paramagnetic above T_C = 42 K. Temperature dependent magnetisation measurements showed an increase in the ordering temperature of the Mn_3O_4 layer to 65 K. However, the expected spacer thickness dependence of the ordering temperature was absent.

3) Across an antiferromagnetic CoO spacer (T_N = 291 K) coupling exists below a CoO thickness of 100 Å. The nature of the coupling can not be determined by means of MOKE due to the change of preferred direction of the magnetisation of the top magnetite layer from in plane to out of plane with increasing CoO thickness for the investigated samples.

The results of the measurements show a wide range of possibilities for coupling of two magnetite layers across a spacer. Unfortunately, the for a spin valve most useful, antiferromagnetic coupling has not been observed in the investigated structures.

The investigation of the Fe_3O_4 / CoO / Fe_3O_4 system deserves further investigation. Using the right combination of substrate and buffer layer could result in a system with a perpendicular magnetisation for all layers. Also the coupling across Mn_3O_4 is interesting for additional investigations. The assumption of proximity magnetism needs to be confirmed.

Further investigation of MBE grown Fe_3O_4 in combination with other materials is necessary to get a better understanding of the magnetic behaviour of these systems. A field hardly unexplored yet is the combination of oxidic / metallic materials. The first study using a non-magnetic Cu spacer did not show the expected polarisation effects. The measured oscillating susceptibility arises from the substrate. However, these hybridic systems might show interesting and useful magnetic behaviour

7. References.

[1] B. Lax and K.J. Button, 'Paramagnetism and Ferromagnetism' in 'Microwave ferrites and ferrimagnets' (McGraw-Hill book company inc., New York, San Francisco, Toronto, London).

[2] E.P.V. Maesen, Graduation report, Group cooperative phenomena EUT (1988).

[3] Q. Zhang and P.M. Levy, Phys. Rev. B **34** (1986) 1884-1898.

[4] Q. Zhang and P.M. Levy, Phys. Rev. B **34** (1986) 7965-7968.

[5] H.A. Kramers, Physica **1** (1934) 182-192.

[6] P.W. Anderson, 'Exchange in insulators' in Magnetism Vol. I, edited by Rado and Suhl, chapter 2 (Academic press, New York and London, 1963).

[7] W. Geertsma, Pysica B **164** (1990) 241-260.

[8] C. Zener, Phys. Rev. **82** (1951) 403-405.

[9] P.G. de Gennes, Phys. Rev. **118** (1960) 141-154.

[10] J.C. Slonczewski, Phys. Rev. B **39** (1989) 6995-7002.

[11] A. Carl and D. Weller, Phys. Rev. Lett. **74** (1995) 190.

[12] L. Néel, Comptes Rendus **255** (1962) 1545.

[13] L. Néel, Comptes Rendus **255** (1962) 1676.

[14] S. Democritov, E. Tsymbal, P. Günberg, W. Zinn and I.K. Schuller, Phys. Rev. B **49** (1994) 720-723.

[15] Y. Suzuki, R.B. van Dover, E.M. Gyorgy, J.M. Phillips and R.J. Felder, Phys. Rev. B **53** (1996) 14017-14019.

[16] J.C. Slonczewski, J. Mag. Mag. Mat. **150** (1995) 13-24.

[17] V.A.M. Brabers, in 'Ferromagnetic materials: a handbook on the properties of magnetically ordered substances', Vol. 8 (Elsevier Science, Amsterdam, 1995).

[18] K. Dwight and N. Menyuk, Phys. Rev. B **119** (1960) 1470-1479.

[19] G.B. Jensen and O.V. Nielsen, J. Phys. C: Solid State Phys. Vol. **7** (1974) 409-424.

[20] Landolt-Börnstein, New Series III / 27g, 6.2.1.

[21] E. Uchida, N. Fukuoka, H. Kondoh, T. Takeda, Y. Nakazumi and T. Nagamiya, J. Phys. Soc. Jpn. **19** (1964) 2088-2095.

[22] R.C. Weast, Handbook on Chemistry and Physics, 54th edition, CRC press, Cleveland (1973-1974).

[23] R.M. Wolf, A.E. de Veirman, P. van der Sluis, P.J. van der Zaag and J.B.F. aan de Stegge, Mater. Res. Soc. Symp. Proc. **341** (1994) 23.

[24] J. Kerr, Phil. Mag. **3** (1877) 339.

[25] R.P. Hunt, J. Appl. Phys. **38** (1967) 1652-1671.

[26] J.J. de Vries, Graduation report, Group cooperative phenomena EUT (1995).

[27] J.M. Florczak and E. Dan Dahlberg, J. Appl. Phys. **67** (1990) 7520-7525.

[28] K. Sato, Jpn. J. Appl. Phys. **20** (1981) 2403-2409.

[29] N.W.E. McGee, Graduation report, Group cooperative phenomena EUT (1991).

[30] M.A. Bongers, Graduation report, Group cooperative phenomena EUT (1995).

[31] J. Hammink, Graduation report, Group cooperative phenomena EUT (1995).

[32] P.A.A. van der Heijden, P.J.H. Bloemen, J.M. Metselaar, R.M. Wolf, J.M. Gaines, J.T.W.M. van Eemeren, P.J. van der Zaag and W.J.M. de Jonge, submitted to Phys. Rev. B.

[33] P.A.A. van der Heijden, J.J. Hammink, P.J.H. Bloemen, R.M. Wolf, M.G. van Opstal, P.J. van der Zaag and W.J.M. de Jonge, Mat. Res. Soc. Symp. Proc. **384** (1995) 27-32.

[34] A.J.G. van Helvoort, Graduation report, Group cooperative phenomena EUT (1995).

[35] J.M. Gaines, P.J.H. Bloemen, J.T. Kohlhepp, R.M. Wolf, A. Reinders, R.M. Jungblut, P.A.A. van der Heijden, J.T.W.M. van Eemeren, J. aan de Stegge and W.J.M. de Jonge, submitted to Surf. Sci.

[36] J. A. Borchers and P.J. van der Zaag, private communications.

[37] A. Carl and D. Weller, Phys. Rev. Lett. **74** (1995) 190-193.

[38] C. Kittel, 'Introduction to solid state physics', 6th edition (Wiley, New York (1986)) 134.

[39] D.L. Camphausen, J.M.D. Coey and B.K. Chakraverty, Phys. Rev. Lett. **29** (1972) 657-660.

[40] A.Yanase and K. Siratori, J. Phys. Soc. Jpn. **53** (1984) 312-317.

8. Appendix.

Calculation of the sign and strength of the coupling due to tunnelling across an MgO spacer.

An estimate will be given of the sign and strength of the coupling for the Fe_3O_4 / MgO / Fe_3O_4 system, based on the theory of coupling via tunnelling of electrons (paragraph 2.2.1 and [10]).

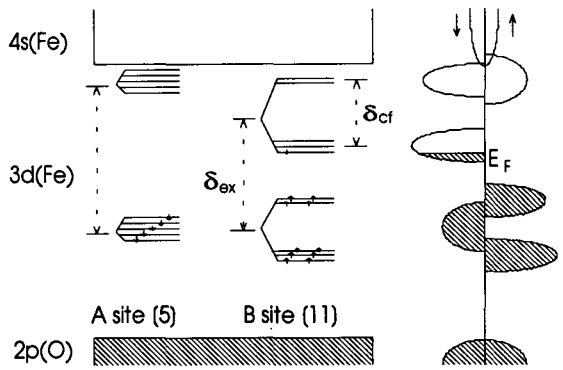

Figure 47. Proposed one-electron model for Fe_3O_4 at room temperature, after [39].

The theory given in paragraph 2.2.1 is according to the one-band model in which only one electron band contributes to the conduction (Figure 10). For magnetite this assumption is correct because the Fermi level lies in a spin down band containing only one electron, and between a completely filled and an empty spin down band. Since the conduction electron is in a spin down band we substitute spin down for spin up and vice versa in the theory of paragraph 2.2.1.

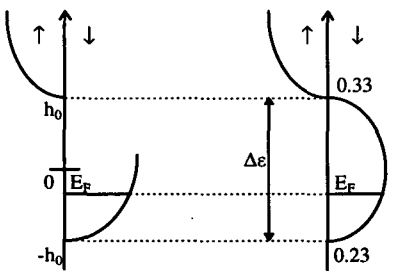

Figure 48. Matching of the band structure according to ref. [10] (left side) and the calculated one by ref. [40] (right side), energies in Ryd.

The band structure as assumed in paragraph 2.2.1 has to be matched to the Fe_3O_4 / MgO / Fe_3O_4 system. In stead of a metallic system, as considered in the original theory, an oxidic

system was investigated. Since the electron wave vectors are unknown they are determined from the energy difference between the top (partially filled) spin down band and the next (empty) spin up band. The band structure for Fe_3O_4 presented in ref. [40] is used. The energy difference ($\Delta\varepsilon$) between the top spin down band (3d band, B site) and the next spin up band (3d band, A site, Figure 47) is 0.10 Ryd. or 1.36 eV. Hence it is possible to determine h_0 to be 0.68 eV (Figure 48). To estimate the position of the Fermi level, the band in which the Fermi level is located is assumed to have a parabolic form (Figure 49).

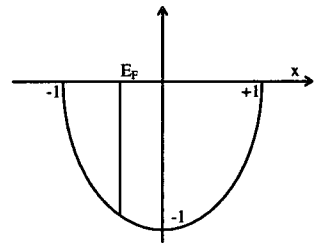

Figure 49. Assumed form of the band in which the Fermi level is located.

The surface under the parabola is given by

$$\int_{-1}^{1}(x^2-1)dx=\left[\tfrac{1}{3}x^3-x\right]_{-1}^{1}=\tfrac{4}{3} \qquad (33)$$

The conduction electron is located at the B-sites (Figure 47). Consider two B-sites, the conduction electron can hop from a Fe^{2+} to a Fe^{3+}, these two ions both contain 5 electrons in a spin up band (3d band), so that the remaining conduction electron has to be positioned in the next spin down band according to Hund's rule. This band is split by the crystal field (δ_{cf} in Figure 47) in a level with two places and a level with three places (Figure 47). So in order to estimate the position of the Fermi level one sixth (two B-sites) of the total surface of the parabola is calculated and the corresponding energy position of the Fermi level is given by

$$\begin{aligned}&\tfrac{1}{3}x^3-x\big|_{-1}-(\tfrac{1}{3}x^3-x)=\tfrac{2}{9}\\&\tfrac{2}{3}-(\tfrac{1}{3}x^3-x)=\tfrac{2}{9}\\&x=-0.48\end{aligned} \qquad (34)$$

This calculation positions the Fermi level $\Delta\varepsilon$*0.52/2=0.354 eV above the lower side of the energy band or at -0.326 eV (Figure 48).
This result enables the calculation of the required parameters using equation (9),(10) to determine the coupling energy with equation (12),(13). The wave vectors are given by

$$\begin{aligned}k_\sigma&=\sqrt{\frac{2m}{\hbar^2}(h_\sigma\sigma+E_F)}, \qquad \sigma=\pm1\\ \kappa&=\sqrt{\frac{2m}{\hbar^2}(U_0-E_F)}\end{aligned} \qquad (35)$$

The energies concerned are: h_0 = 0.680 eV, E_F = -0.326 eV and the energy difference U_0 - E_F = 1.75 eV for the MgO / Fe_3O_4 system. The last value has been calculated by

comparing the energy band structure of MgO with that of Fe_3O_4 by using the vacuum level as a reference. The effective electron mass is not known for this system so the standard electron mass is used. Using these energies, the resulting values for the wave vectors are $k_{\downarrow} = 0.305$ Å^{-1} , $k_{\uparrow} = i\,0.530$ Å^{-1}, $\kappa = 0.678$ Å^{-1} . So that $2\kappa = 1.36$ Å^{-1} and $J_0 = -18$ meV This results in an anti-parallel coupling because if J is negative, the exchange coupling energy -J cos θ will be positive so that in order to achieve the lowest energy the two magnetisation vectors will prefer an angle 180^0 in order to minimise the energy (< 0). This can also be seen in Figure 11, with $\kappa^2 / k^2_{\downarrow} = 4.94$ and the ratio $k_{\uparrow} / k_{\downarrow} = 2.22i$ the exchange coupling energy will be negative.

9. Acknowledgements.

I would like to thank the following people who made my graduation period a pleasant one:

Paul van der Heijden, my supervisor and the person I worked closest with.
Pieter Jan van der Zaag, my supervisor from Philips.
Wim de Jonge, my professor and the one who made this graduation work possible.

Jasper, Martin, Erik, Johan, Jim, Jitze Jan, Pascal, Robert, Theo, William, Ralph, Christine, Bart and all the other people I worked with and joined for lunch and coffee breaks.

Bert, Jannie, Janneke and other close family for the support during the time of my study.

Jeroen, Alex, Seth and all the other members or former members of the Dispuut Astarte for the good times we had, and will have.

Everybody I forgot to thank, probably a lot of people.